Chemical Engineering Science 259 (2022) 117791

Contents lists available at ScienceDirect

Chemical Engineering Science

journal homepage: www.elsevier.com/locate/ces

A phase-change model for diffusion-driven mass transfer problems in incompressible two-phase flows

Gabriele Gennari, Richard Jefferson-Loveday, Stephen J. Pickering

Department of Mechanical, Materials and Manufacturing Engineering, University of Nottingham, Nottingham NG7 2RD, United Kingdom

HIGHLIGHTS

- The two-scalar method for species transport is coupled with a geometric VOF solver.
- A novel algorithm is presented to extend the liquid velocity field at the interface.
- Study of growing bubbles on electrodes with different contact angles and currents.

ARTICLE INFO

Article history:
Received 1 March 2022
Received in revised form 4 May 2022
Accepted 6 June 2022
Available online 17 June 2022

Keywords:
Multiphase Flow
Interfacial mass transfer
Volume of Fluid
Henry's Law
Bubbly flows

ABSTRACT

We present a VOF-based numerical method for incompressible Direct Navier–Stokes (DNS) equations for diffusion-driven phase-change flows. A special emphasis is placed on the treatment of velocity discontinuities across the interface. A novel algorithm is presented to smoothly extend the liquid velocity field across the interface in a way that the interface can be transported by a divergence-free velocity field. The transport of species is treated with a two-scalar approach and special attention is paid to the advection and diffusion steps in order to prevent artificial mass transfer. The methodology is implemented in the open-source code Basilisk and is validated against analytical and semi-analytical models. The relative errors on the relevant quantities are generally below 1% for the finest grids. The method is finally applied to study the growth of electrochemically generated bubbles on planar electrodes and the effect of contact angles and number of nucleation sites is investigated.

1. Introduction

Mass transfer phenomena driven by diffusion of chemical species occur in a variety of industrial applications which involve two-phase gas–liquid systems, such as bubble column reactors, waste-water treatment facilities, photo- and electro- chemical reactors and many others. In order to improve the design and efficiency of such systems, a number of details about the characteristic flow features are needed. In the case of bubbly flows, the typical size of bubbles, their distribution within the reactor, rising velocities, mass transfer rates and induced mixing within the vessel are just a few physical flow features that are extremely relevant for the optimization of these devices. However, analytical solutions for this class of problem are not generally available and only a few exact solutions can be derived using extremely simplified assumptions (Epstein and Plesset, 1950; Scriven, 1959; Clift et al., 1978). Although these models are not applicable to the design of real systems, they still provide useful information and reference solutions for the validation of other models (e.g. numerical approaches). Experimental methods have been successfully used to investigate the mass transfer and rising velocities of bubbles (Takemura and Yabe, 1998; Takemura and Yabe, 1999; Takemura and Matsumoto, 2000) and advanced visualization techniques have been employed to investigate the gas concentration released in the liquid by bubbles (Dani et al., 2007; Francois et al., 2011). However, experimental measurements are generally expensive and limited by the available measuring techniques which usually provide global quantities (e.g. global mass transfer rate, rising velocities) and do not give information about local details, such as local mass transfer rates. On the other hand, the continuous increase in computational power and the development of High-Performance-Computing (HPC) facilities make high-fidelity numerical simulations a valuable alternative to investigate the detailed dynamics of mass transfer across deformable interfaces. Among the most popular numerical methods for two-phase flows are the Front Tracking (FT) approach (Tryggvason et al., 2001), the Level Set (LS) method (Sussman et al., 1994) and the Volume Of Fluid (VOF) approach (Hirt and Nichols, 1981; Scardovelli and Zaleski,

https://doi.org/10.1016/j.ces.2022.117791
0009-2509/

1999). The VOF method has been applied successfully to a variety of multi-phase problems with complex interfaces and one of its major strengths is the capability to preserve mass. The present work focuses on the coupling of the VOF method with the transport of chemical species for phase-change problems, where the mass transfer is driven by the concentration of species. Examples of published works which employ the VOF method to study phase-change of incompressible flows (both temperature- or concentration-driven) can be found in (Welch and Wilson, 2000; Schlottke and Weigand, 2008; Kunkelmann and Stephan, 2009; Magnini et al., 2013; Ma and Bothe, 2013; Fleckenstein and Bothe, 2015; Vachaparambil and Einarsrud, 2020; Taqieddin et al., 2020; Maes and Soulaine, 2020; Scapin et al., 2020; Malan et al., 2021; Zanutto et al., 2022a; Zanutto et al., 2022b). It is worth pointing out that although temperature-driven (e.g. boiling, evaporation) and concentration-driven (e.g. absorption, desorption) phenomena have different mechanisms which drive the mass transfer (i.e. temperature vs concentration), the mathematical formulation of the governing equations (i.e. continuity and conservation of momentum) is the same and the numerical schemes derived for the first class of problems can be applied to the second type of flows. Although many studies have been published on the numerical modelling of incompressible phase-change problems by means of the VOF method, only a few of them have combined a rigorous treatment of the velocity jump across the interface, which occurs when mass is transferred between phases with different densities, with a sharp advection of the interface. In the work of Schlottke and Weigand (2008), the authors derived an iterative method to compute a virtual velocity field based on the interface and gas velocities which fulfills the continuity constraint. More recently, Malan et al. (2021) proposed an approach to extend the liquid velocity field across the interface of evaporating droplets, in a way that the resulting flow velocity is divergence-free everywhere. This extended velocity was then used to transport the interface. This point is fundamental when dealing with geometric VOF schemes designed for incompressible flows, which generally ensure mass conservation, provided the velocity field is divergence-free everywhere (an example of such schemes can be found in Weymouth and Yue (2010)). Similar methods to Malan et al. (2021) are proposed in Scapin et al. (2020) and Guo (2020) for evaporating and boiling flows. Such treatments of velocity discontinuities at the interface are particularly relevant for large mass transfer rates, where significant convective (Stefan) flows are expected. The previous methods rely on iterative algorithms (Schlottke and Weigand, 2008) or on the solution of an additional elliptic equation (Malan et al., 2021; Scapin et al., 2020; Guo, 2020). In the present work we contribute to the treatment of interfacial velocity discontinuities by proposing an original algorithm which does not require the solution of additional partial differential equations and is readily implementable in existing VOF codes. The goal is the same as the method proposed by Malan et al. (2021), i.e. to obtain a divergence-free liquid velocity field for the transport of the interface. The method is coupled with a geometric VOF scheme based on the Piecewise Linear Interface Construction (PLIC) method.

The transport of chemical species in two-phase flow systems adds additional challenges for numerical methods, as the concentration is generally discontinuous across the interface due to different solubilities in the gas and liquid phases. In this work, the jump in species concentration across the interface is modeled by applying Henry’s Law. Two main approaches are available for the transport of species and can be classified as one-scalar and two-scalar methods, according to the number of equations which are solved for each species. Among the one-scalar approaches, we remind of the work of Bothe et al. (2004) where the concentration field is represented by a single scalar which is made continuous across the interface by applying a proper variable transformation. For others methods based on similar scaling procedures, the reader is referred to the references in Bothe and Fleckenstein (2013). A different approach within the one-scalar family is presented in Haroun et al. (2010), where the species transport equation is derived from the one-fluid formulation of the concentration field. The result is an additional diffusive-like term which represents the concentration jump at the interface. This method is further discussed and extended in Marschall et al. (2012),Deising et al. (2016) (Continuous Species Transfer model - CST) and Maes and Soulaine (2018) (Compressive Continuous Species Transport method - C-CST). The method of Haroun et al. (2010) and the C-CST approach are used to study the growth of rising bubbles in supersaturated solutions in Taqieddin et al. (2020) and Vachaparambil and Einarsrud (2020), respectively; the C-CST model is also employed in Maes and Soulaine (2020) for multicomponent mass transfer problems. One-scalar methods are further developed in the works of Zanutto et al. (2022a) and Zanutto et al. (2022b), where an algebraic VOF method is coupled with the CST model. The authors show the importance of treating the advection of the interface and concentration field with the same numerical scheme in order to preserve mass; the method is validated for evaporating flows and non-ideal mixtures with large jumps in the concentration profiles across the interface. Among the two-scalar methods, we recall the work of Alke et al. (2009) where the concentration is represented by two one-sided (i.e. confined to one side of the interface) scalars, which are extended to zero in the other phase. These VOF-like variables can be transported (advection) using the same fluxes as used for the phase volume fraction field. The mass transfer appears as a source term which is simultaneously added and subtracted from the transport equations, so that the method is inherently mass conservative. This method requires the direct evaluation of the mass transfer term for each interfacial cell (contrary to one-scalar approaches) and different approaches for this term are compared in Bothe and Fleckenstein (2013). This methodology is further extended in Fleckenstein and Bothe (2015) for multicomponent mass transfer with volume change. A novel implementation of the two-scalar method is presented in Schulz et al. (2022), where the authors use the PLIC reconstruction of the interface to split the mesh between the phases. The newly created cell faces match the interface and accurate boundary conditions can be set for the transport of species. A hybrid method was recently proposed by Kumar Farsoiya et al. (2021) for geometric VOF schemes, which uses the one-scalar approach of Haroun et al. (2010) for the diffusion step and recovers the two-scalar formulation for the advection of the species concentration. As pointed out by Deising et al. (2016) the choice between the one- or two-scalar approaches depends on the type of VOF methodology used. For algebraic VOF methods, the most convenient choice is the one-scalar approach, where the consistency in the treatment of the interface and species advection is a crucial point to ensure mass conservation (Zanutto et al., 2022a). In this work we use a geometric VOF scheme and the natural way to transport the species is the two-scalar method, where the PLIC-based fluxes are used to advect the two scalars. This ensures that the concentration fields are kept confined to their respective phase during the transport of the interface and prevents the occurrence of artificial mass transfer. In the present paper we implement the method of Fleckenstein and Bothe (2015) in the open source code Basilisk (http://basilisk.fr/) for pure gas bubbles which exchange mass with the surrounding liquid and we provide the details of the implementation; particular attention is devoted to the integration of the species transport and VOF equations and the relative velocity extension algorithm.

The work is organized as follows. The governing equations and the one fluid formulation which leads to the VOF model are introduced in Section 2. The details of the numerical implementation of the phase-change model are given in Section 3, while the methodology is validated in Section 4 against analytical and semi-analytical solutions for 2D and 3D problems. Finally, the methodology is applied to the study of growing bubbles on planar electrodes in Section 5.

2. Governing Equations

We consider the two-phase gas–liquid system represented in Fig. 1. Although the methodology presented in this work can be applied to a generic multi-phase flow, we mainly focus on disperse bubbly flows and we refer to the gas and liquid phases as disperse and continuous phases respectively. The regions occupied by the two phases are called $\Omega_d(t)$, for the disperse phase, and $\Omega_c(t)$ for the continuous phase, and these two sub-domains are separated by an infinitely thin interface $\Sigma(t)$, so that the entire domain is given by $\Omega = \Omega_d(t) \cup \Omega_c(t) \cup \Sigma(t)$. We define the normal vector ($\mathbf{n}_\Sigma$) at the interface as the unit vector which points into $\Omega_d(t)$. To simplify the notation, in the following we omit the time dependence from the phase domains (Ω_d, Ω_c) and interface (Σ). The terms continuous (disperse) and liquid (gas) will be used interchangeably in the rest of the work.

2.1. Two-phase Navier–Stokes equations

For each phase, the system of governing laws for an incompressible flow is given by the Navier–Stokes equations:

$$\nabla \cdot \mathbf{u} = 0 \ \text{in} \ \Omega \setminus \Sigma \tag{1}$$

$$\partial_t(\rho \mathbf{u}) + \nabla \cdot (\rho \mathbf{u} \otimes \mathbf{u}) = -\nabla p + \nabla \cdot (2\mu \mathbf{D}) + \rho \mathbf{a} \ \text{in} \ \Omega \setminus \Sigma \tag{2}$$

where the material properties, e.g. density (ρ) and viscosity (μ), have constant values in Ω_d, Ω_c and depend on the respective phase. Eq. 1 is the continuity equation (balance of mass), where $\mathbf{u}$ represents the fluid velocity field. In the balance of momentum (Eq. 2), p is the static pressure, $\mathbf{a}$ contains the acceleration terms which come from external body forces (e.g gravitational force) and $\mathbf{D}$ is the deformation tensor $\left[\nabla \mathbf{u} + (\nabla \mathbf{u})^T\right]/2$. The only body force which is considered in the present work is the gravitational force; the acceleration term $\mathbf{a}$ is then replaced by $\mathbf{g}$ in the following sections. Eqs. 1 and 2 are valid everywhere in the domain, except at the interface, where additional conditions are needed to close the system (see Tryggvason et al., 2011). The first condition derives from the principle of mass conservation and states that the amount of mass which leaves Ω_d (Ω_c) must be entirely transferred to Ω_c (Ω_d) since the interface is an infinitely thin region and no mass can be stored in it. This statement results in a jump condition across the interface for the normal component of the velocity field:

$$\|\rho(\mathbf{u} - \mathbf{u}_\Sigma) \cdot \mathbf{n}_\Sigma\| = \|\dot{m}\| = 0 \tag{3}$$

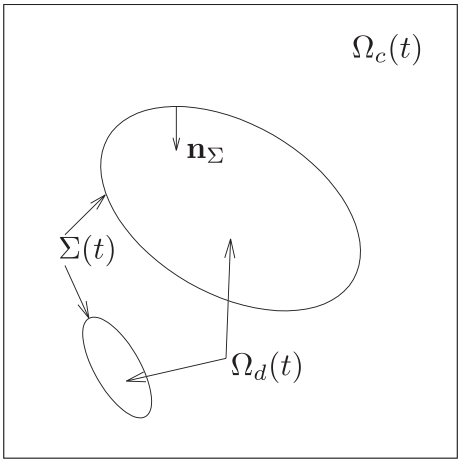

Fig. 1. Two-phase gas–liquid domain.

where the jump notation has been introduced (e.g. $\|\rho\| = \rho_c - \rho_d$); $\mathbf{u}_\Sigma$ is the interface velocity and $\dot{m}$ is the mass transfer rate [kg/m^{2}s]. Eq. 3 is also known as the Rankine-Hugoniot condition and for flows without phase-change ($\dot{m} = 0$) it implies that no relative velocity along the normal direction can occur between the fluids and the interface. The second jump condition can be derived by applying the conservation of momentum to a control volume with an infinitely small thickness around the interface and it reads:

$$\|\rho \mathbf{u} \otimes (\mathbf{u} - \mathbf{u}_\Sigma) + p\mathbf{I} - 2\mu \mathbf{D}\| \cdot \mathbf{n}_\Sigma = \sigma k \mathbf{n}_\Sigma + \nabla_\Sigma \sigma \tag{4}$$

where $\mathbf{I}$ is the unit tensor, σ is the surface tension and k is the curvature of the interface. In the present work we focus on gas bubbles which exchange mass with the surrounding liquid (e.g. water) and we consider interfaces with uniform surface tension. Given the physical properties of these types of flow and assuming a no-slip condition for the tangential velocities at the interface (coherently with the assumption of phases with non-vanishing viscosity), Eq. 4 can be further simplified to (see Fleckenstein and Bothe, 2015):

$$\|p\mathbf{I} - 2\mu \mathbf{D}\| \cdot \mathbf{n}_\Sigma = \sigma k \mathbf{n}_\Sigma \tag{5}$$

The numerical approach used in the present work for the transport of the interface is the VOF method, which relies on the so-called one-fluid formulation of the governing equations. In the one-fluid approach we solve a single set of Navier–Stokes equations for the entire domain Ω and the jump conditions (Eqs. 3 and 4) are replaced by source terms that act at the interface as singularities (δ- functions). The one-fluid formulation of the Navier–Stokes equations for incompressible flows reads:

$$\nabla \cdot \mathbf{u} = \dot{m}\left(\frac{1}{\rho_d} - \frac{1}{\rho_c}\right)\delta_\Sigma \tag{6}$$

$$\partial_t \mathbf{u} + \nabla \cdot (\mathbf{u} \otimes \mathbf{u}) = \frac{1}{\rho}[-\nabla p + \nabla \cdot (2\mu \mathbf{D})] + \mathbf{g} + \frac{\sigma k \mathbf{n}_\Sigma}{\rho}\delta_\Sigma \tag{7}$$

where δ_Σ is the surface Dirac function which has a nonzero value only at the interface and the last term on the right-hand side of Eq. 7 is the surface tension force per unit volume, written in the volumetric formulation. The material properties (i.e. density and viscosity) assume different values in the respective phase and are discontinuous across the interface. The system of Eqs. 6 and 7 is valid in the whole domain and it recovers the form of Eqs. 1,2 in the region $\mathbf{x} \notin \Sigma$, where $\delta_\Sigma = 0$. In the one-fluid approach we need a marker function to determine the location of the interface and to identify whether a point $\mathbf{x} \in \Omega_c$ or Ω_d; a transport equation for this function can then be derived to track the position of the interface. The Heaviside function serves this purpose:

$$H(\mathbf{x}, t) = \begin{cases} 1, & \text{if } \mathbf{x} \in \Omega_c \\ 0, & \text{if } \mathbf{x} \in \Omega_d \end{cases} \tag{8}$$

Once $H(\mathbf{x}, t)$ is known everywhere, the values of ρ and μ in Eq. 7 can be computed as:

$$\rho = \rho_c H + \rho_d(1 - H) \tag{9}$$

and

$$\mu = \mu_c H + \mu_d(1 - H) \tag{10}$$

where the arithmetic mean has been used (different formulations are clearly possible, e.g. the harmonic mean). The transport equation for $H(\mathbf{x}, t)$ is obtained from the following integral balance for a control volume V:

$$\int_V \partial_t H \, dV + \oint_{\partial V} H\mathbf{u} \cdot \mathbf{n} \, dS + \int_\Sigma (\mathbf{u}_c - \mathbf{u}_\Sigma) \cdot \mathbf{n}_\Sigma \, dS = 0 \tag{11}$$

where the second term represents the convective transport and the last term accounts for the mass transfer across the interface. Converting the surface integrals to volume integrals, Eq. 11 can be written in the differential form:

$$\partial_t H + \nabla \cdot (H\mathbf{u}) + \frac{\dot{m}}{\rho_c} \delta_\Sigma = 0 \tag{12}$$

Eq. 12 is the starting point for the derivation of the Volume of Fluid method (see Section 3.2).

2.2. Transport of species

In a generic two-phase system both phases can be a mixture of several chemical species. For the generic species k, the individual mass balance reads:

$$\partial_t \rho^k + \nabla \cdot (\rho^k \mathbf{u}^k) = R^k \tag{13}$$

where ρ^k is the partial density, $\mathbf{u}^k$ denotes the species velocity and R^k is a generic reaction term that can be used to model chemical reactions. Eq. 13 is coupled with the jump condition at the interface for conservation of mass:

$$\| \rho^k (\mathbf{u}^k - \mathbf{u}_\Sigma) \cdot \mathbf{n}_\Sigma \| = \| \dot{m}^k \| = 0 \tag{14}$$

The average phase density and velocity that appear in the Navier–Stokes Eqs. 6,7 are derived from the respective species terms as:

$$\rho = \sum_k \rho^k \tag{15}$$

and

$$\rho \mathbf{u} = \sum_k \rho^k \mathbf{u}^\mathbf{k} \tag{16}$$

Taking advantage of Eq. 16, the individual mass balance of species k (Eq. 13) for incompressible flows can be rewritten as:

$$\partial_t \rho^k + \mathbf{u} \cdot \nabla \rho^k + \nabla \cdot \mathbf{J}^k = R^k \tag{17}$$

where the diffusive flux is introduced:

$$\mathbf{J}^k = \rho^k (\mathbf{u}^k - \mathbf{u}) \tag{18}$$

The mass transfer rate of a single species can be rearranged using Eq. 14 into:

$$\begin{aligned} \dot{m}^k &= \rho^k (\mathbf{u}^k - \mathbf{u}_\Sigma) \cdot \mathbf{n}_\Sigma \\ &= \rho^k (\mathbf{u} - \mathbf{u}_\Sigma) \cdot \mathbf{n}_\Sigma + \rho^k (\mathbf{u}^k - \mathbf{u}) \cdot \mathbf{n}_\Sigma \\ &= \tfrac{\rho^k}{\rho} \dot{m} + \mathbf{J}^k \cdot \mathbf{n}_\Sigma \end{aligned} \tag{19}$$

which shows that for each chemical component, the mass transfer contains both a convective term and a diffusive term. Under the assumption of dilute liquid solutions, the diffusive flux (Eq. 18) can be well modelled by Fick's law of diffusion:

$$\mathbf{J}^k = -D^k \nabla \rho^k \tag{20}$$

where D^k is the species coefficient of diffusion which assumes different but constant values for each phase. Although the methodology employed in this work can be applied to multi-component species transfer, in the present study we focus on pure incompressible gas bubbles and we assume that no liquid species exists in the disperse phase (i.e. the liquid is not volatile). Therefore, the system contains two different species: pure gas ($k = 1$) and liquid ($k = 2$) and the overall mass transfer ($\dot{m}$) is entirely given by the transfer rate of the single species which exists in the disperse phase, i.e. $\dot{m} = \dot{m}^1$. It is worth pointing out that we do not need to solve the individual mass balance (Eq. 17) in the disperse region, since no mixture exists inside the bubbles (pure gas) and the density is assumed to be constant everywhere in Ω_d. Combining Eqs. 19,20, the mass transfer rate for a single species system reads:

$$\dot{m} = -\frac{M^1 D^1}{1 - \rho^1/\rho} \frac{\partial c^1}{\partial \mathbf{n}_\Sigma} \tag{21}$$

where the molar concentration has been introduced, i.e. $c^1 = \rho^1/M^1$ and M^1 is the molar mass. Eq. 21 gives the mass transfer rate evaluated from the continuous side of the interface, where the concentration of the dissolved species is generally variable. According to the jump condition for mass conservation (Eq. 14), the same amount of mass must be transferred from the disperse side of the interface ($\dot{m}_c = \dot{m}_d$). However, for the applications considered in this work (pure incompressible bubbles), solving Eq. 19 in Ω_d, where $\rho = \rho_d =$ const, simply gives the identity $\dot{m} = \dot{m}$. Therefore, in order to compute the value of $\dot{m}$, Eq. 21 must be computed in Ω_c. Since we have only one species which can be transferred between phases, in the following we will omit the species indicator k as we will always refer to the concentration of the soluble species.

For a gas–liquid system at equilibrium, we can employ Henry's law to compute the concentration on the liquid side of the interface, which is directly proportional to the partial pressure of gas on the liquid. Taking advantage of the perfect gas law, we can write Henry's formula in terms of a jump condition for the species concentration at the interface:

$$(c_c)_\Sigma = \frac{(c_d)_\Sigma}{He} \tag{22}$$

where He is the Henry coefficient and it is a material property of the gas–liquid system, which generally depends on the temperature and pressure fields near the interface. For the applications considered in the present work, He is assumed to be constant (see Bothe and Fleckenstein, 2013). The interface is considered to be at equilibrium and the liquid-side of gas concentration is immediately known from Eq. 22, where $(c_d)_\Sigma = \rho_d/M$. Henry's law will be used for the computation of the gradient term in the mass transfer rate formula (Eq. 21) and the relative discretization scheme is introduced in Section 3.4.

In order to obtain a system of transport equations suitable for the numerical integration of the two-scalar approach of Bothe and Fleckenstein (2013), we need to rewrite the individual mass balance (Eq. 17) in a form where the mass transfer rate appears explicitly. Here we do this in Ω_c only, for a non reactive flow ($R = 0$), and we start from the following integral balance for the species concentration:

$$\int_V \partial_t c_c \, dV + \oint_{\partial V} (c_c \mathbf{u}_c - D_c \nabla c_c) \cdot \mathbf{n} \, dS + \int_\Sigma c_c (\mathbf{u}_c - \mathbf{u}_\Sigma) \cdot \mathbf{n}_\Sigma \, dS = 0 \tag{23}$$

By combining Eqs. 23 and 14 we get the final differential form of the species transport equation:

$$\partial_t c_c + \mathbf{u}_c \cdot \nabla c_c - \nabla \cdot (D_c \nabla c_c) = -\frac{\dot{m}}{M} \delta_\Sigma \tag{24}$$

where the incompressible velocity constraint has been applied ($\nabla \cdot \mathbf{u}_c = 0$). Since we treat single species transfer problems, the gas dissolved in Ω_c is the only species for which we need to solve the respective transport Eq. (24); therefore, in the following, we will omit the phase indicator, i.e. $c = c_c$.

3. Numerical Method

The numerical framework used to solve the governing equations shown in Section 2 is the open source solver Basilisk

(Popinet and collaborators, 2013–2022), which is a Finite Volume (FV) solver platform for adaptive Cartesian grids. The ability of refining the mesh at each iteration (Adaptive Mesh Refinement technique - AMR) in regions where strong gradients occur makes Basilisk a suitable software for interfacial flows where, generally, a fine grid is required around the gas–liquid interface (but not everywhere in the domain). The shape of the domain is always a square (cube) in 2D (3D) and the grid is organized following a hierarchical quadtree (octree) structure. Each cell can be further divided into four children cells (eight in 3D) and a level is assigned to each cell, following the relative tree structure. The root cell is the only cell present at level zero and the dimension of a generic cell at level n is given by $\Delta = L0/2^n$, where $L0$ is the length of the whole computational domain. For a detailed description of the mesh structure and relative nomenclature, the reader is referred to Popinet (2003).

In this Section, a brief description of the numerical methodology is provided. Section 3.1 outlines the time integration of the Navier–Stokes equations, while the VOF method is described in Section 3.2. Here we introduce a new approach to make incompressible VOF schemes compatible with phase-change flows, where $\nabla \cdot \mathbf{u} \neq 0$ at $\mathbf{x} \in \Sigma$. The integration of the Species Transport Eq. (24) and the computation of the mass transfer term $(\dot{m})$ are finally described in Sections 3.3 and 3.4, respectively.

3.1. Navier–Stokes solver

The approach used to solve the Navier–Stokes equations is a time-splitting pressure-correction method, which is second order accurate in time and space. For a general description of the algorithm, the reader is referred to Sharaborin et al. (2021); more details on a similar scheme can be found in Popinet (2003) and Popinet (2009). The VOF field, along with any other tracer (e.g. the species concentration field), is first integrated from time $t_{n-\frac{1}{2}}$ to $t_{n+\frac{1}{2}}$ and the fluid properties (i.e. density and viscosity) are updated. The momentum Eq. (7) is then discretized without taking into account the pressure gradient term:

$$\rho_{n+\frac{1}{2}}\left[\frac{\mathbf{u}_* - \mathbf{u}_n}{\Delta t} + \nabla \cdot \left(\mathbf{u}_{n+\frac{1}{2}} \otimes \mathbf{u}_{n+\frac{1}{2}}\right)\right] = \nabla \cdot \left(2\mu_{n+\frac{1}{2}}\mathbf{D}_*\right) + \mathbf{g} + (\sigma k \mathbf{n}_\Sigma \delta_\Sigma)_{n+\frac{1}{2}} \tag{25}$$

where $\Delta t = t_{n+1} - t_n$. The first step is the integration of the convection term, which requires a prediction of the velocity field at time $t_{n+\frac{1}{2}}$. This is done using the unsplit, upwind second order scheme of Bell et al. (1989), which extrapolates the face-centered velocity field from the known cell-centered velocities at time t_n, taking into account the effect of the pressure gradient, surface tension and gravitational acceleration. The obtained face velocity field is generally non-divergence free and a projection step is applied to enforce the continuity constraint. The convective term in Eq. 25 is then integrated by transporting the cell-centered velocity field $(\mathbf{u}_n)$ with the same advection scheme of Bell et al. (1989).

The next step is the integration of the viscous term which is performed implicitly with a second order central differential scheme. A multigrid algorithm is used to efficiently solve the viscous equation and restriction and prolongation operators are defined in order to transfer the solution from the finer and coarser meshes, respectively. The hierarchical structure of the Cartesian grid in Basilisk offers a natural environment for the implementation of the multigrid solver and more details can be found in Popinet (2015).

The velocity $\mathbf{u}_*$ is then obtained by adding the contribution of the gravitational and surface tension forces. The last term is discretized following the approach proposed by Brackbill et al. (1992), which consists in the following approximation:

$$\left(\frac{\sigma k \mathbf{n}_\Sigma \delta_\Sigma}{\rho}\right)_{n+\frac{1}{2}} = \left(\frac{\sigma k \nabla f}{\rho}\right)_{n+\frac{1}{2}} \tag{26}$$

where f is the volume fraction field (defined in Section 3.2). Special attention is given to the discretization of the term ∇f, which is approximated with the same scheme used for the gradient of pressure. This is fundamental to guarantee that the equilibrium solution of the Laplace equation (i.e. the equilibrium between pressure and surface tension across the interface of a stationary spherical bubble/droplet) is verified by the numerical approach. A method which satisfies such requirement is generally defined as a well-balanced method and it is fundamental to reduce the magnitude of spurious currents. The volumetric formulation of the surface tension force (Eq. 26) requires the computation of the interface curvature k, which is generally a challenging task for VOF methods. Basilisk implements a height function (HF) approach where the location of the interface (height) is first obtained from the summation of the volume fraction field over few cells and then is differentiated in order to compute the curvature. In the case of low mesh resolution or highly curved interfaces, the HF method could fail to find a suitable interfacial height; in this case a parabolic function is fitted through the interface and the curvature is obtained by differentiating the resulting formula. For a review about numerical methods to treat surface tension problems, the reader is referred to Popinet (2018) and to Popinet (2009) for a detailed description of the HF algorithm.

To obtain the velocity at the end of the time step $(\mathbf{u}_{n+1})$, we need to take into account the contribution of the pressure gradient:

$$\rho_{n+\frac{1}{2}}\left[\frac{\mathbf{u}_{n+1} - \mathbf{u}_*}{\Delta t}\right] = -\nabla p \tag{27}$$

By applying the continuity constraint (Eq. 6) we get the Poisson equation for pressure at time t_{n+1}:

$$\nabla \cdot \left(\frac{\Delta t}{\rho_{n+\frac{1}{2}}}\nabla p\right) = \nabla \cdot \mathbf{u}_* - \dot{m}_{n+\frac{1}{2}}\left(\frac{1}{\rho_d} - \frac{1}{\rho_c}\right)\left(\frac{A_\Sigma}{V}\right)_{n+\frac{1}{2}} \tag{28}$$

where the δ-function which appears on the RHS of Eq. 6 is already shown in its FV formulation, i.e. the ratio between the interfacial area A_Σ (computed for each interfacial cell based on the reconstructed PLIC element) and the cell volume V (see Fleckenstein and Bothe, 2015). Once the pressure is obtained from Eq. 28, the velocity $\mathbf{u}_{n+1}$ is computed from Eq. 27. An analogous step is performed during the integration of the convective term, but with a time step of $\Delta t/2$ instead of Δt.

The time step integration ends with the adaption of the mesh, where the grid can be refined/coarsened according to a wavelet-based estimation of the spatial discretization error for specific fields (e.g. velocity, volume fraction and gas concentration fields). The reader is referred to van Hooft et al. (2018) for details about the AMR technique.

3.2. Volume of Fluid method (VOF)

The starting point for the derivation of the VOF method is the definition of the volume fraction for the continuous phase:

$$f_c = \frac{\int_V H \, dV}{V} \tag{29}$$

where V is the computational cell volume. For a cell completely filled with liquid $f_c = 1$; if the cell is pure gas $f_c = 0$, while for interfacial cells $0 < f_c < 1$. The volume fraction of the disperse phase is known from the relationship $f_c + f_d = 1$. Therefore, we don't need to solve an additional equation for f_d and, in the following, we will omit the phase indicator ($f = f_c$). Eq. 12 can then be rewritten in the following form:

$$\frac{f_{n+\frac{1}{2}}-f_{n-\frac{1}{2}}}{\Delta t}+\frac{1}{V}\int_V \nabla\cdot(H\mathbf{u})\,dV+\frac{1}{V}\int_V \frac{\dot{m}}{\rho_c}\delta_\Sigma\,dV=0 \tag{30}$$

The integration of Eq. 30 is performed in two steps: first, f is advected by the liquid velocity field and then the interface is shifted to take into account the mass transfer term.

3.2.1. Step 1. The advection term

The advection term is integrated with a geometric scheme based on the Piecewise Linear Interface Construction (PLIC) method, where the interface is reconstructed as a line (plane) in 2D (3D). For each interfacial cell we can define a local reference system centered on the cell centroid and the interface is then described by the following equation (see Fig. 2 for a 2D example):

$$xn_{\Sigma x}+yn_{\Sigma y}+zn_{\Sigma z}=\alpha \tag{31}$$

where the components of $\mathbf{n}_\Sigma$ are such that $|n_{\Sigma x}|+|n_{\Sigma y}|+|n_{\Sigma z}|=1$ and the spatial dimensions are scaled with the cell length Δ. The integration of the advection term is performed in two steps, namely the reconstruction step and the propagation step (Scardovelli and Zaleski, 1999). During the reconstruction step, the interface normal $\mathbf{n}_\Sigma$ is computed by combining the schemes of Youngs (1984) and the centered-columns method (Tryggvason et al., 2011). Once $\mathbf{n}_\Sigma$ is known, α is uniquely determined from $f_{n-\frac{1}{2}}$ and $\mathbf{n}_\Sigma$. The second step consists of computing the geometrical fluxes for each pair of cell faces, i.e. the quantity of volume fraction which is transported across each pair of boundaries during the time step integration. Taking adavantage of the interface reconstruction, the exact volume (in the sense of the PLIC approximation) of continuous phase which is transported from cell (i,j) to the cell on the right $(i+1,j)$ can be computed, as shown in Fig. 3, where the face-centered velocity $u_x|_{i+\frac{1}{2}}$ is assumed to be positive, i.e. it points towards the cell neighbour on the right side. The advection step is finally performed using the operator-split scheme proposed by Weymouth and Yue (2010), where the volume fraction is updated by applying the VOF fluxes in a sequential manner along the x, y and z directions. To minimize errors, the order of the advection steps is changed at each iteration. The method of Weymouth and Yue (2010) is exactly mass conservative, provided the velocity field is divergence free, which is the typical situation for incompressible flows without mass transfer. However, this is not the case for two-phase gas–liquid flows with phase-change, where $\nabla\cdot\mathbf{u}\neq 0$ at $\mathbf{x}\in\Sigma$, as given by the continuity Eq. (6). A possible solution to this problem comes from the observation that the volume fraction field f is advected by the continuous phase velocity only and, therefore, the solenoidal requirement of the VOF scheme applies only to the same velocity component. Integrating the advection term of Eq. 30 on a computational cell reads:

$$\frac{f_*-f_{n-\frac{1}{2}}}{\Delta t}=-\frac{1}{V}\int_V \nabla\cdot(H\mathbf{u}_c)\,dV \tag{32}$$

where $\mathbf{u}$ has been replaced by $\mathbf{u}_c$ to emphasize the point that the Heaviside function is transported by the liquid phase only. Therefore, the idea to make the incompressible VOF scheme compatible with phase-change flows is to find a consistent way to extend the liquid velocity field across the gas–liquid interface, so that for each cell where $f>\epsilon$, the divergence of the velocity field is null (ϵ is a threshold value used to identify the cells which contain liquid and is set to 10^{-6}); we refer to the extended velocity field as $\mathbf{u}_{c,ext}$. At this point, a remark is in order. Such a correction algorithm should be able to preserve the velocity field in pure liquid/gas cells (where $\mathbf{u}$ is already divergence free) and modify $\mathbf{u}$ in interfacial cells only. However, a solenoidal extension requires a velocity correction in a few neighbouring (pure) cells too; these cells must be pure gas ones, as we need to preserve $\mathbf{u}_c$ in liquid cells during the transport of the volume fraction field. Although developed for different reasons, several approaches exist to extend phase velocity fields in multiphase flows. The Ghost Fluid method (Fedkiw et al., 1999) is the basis for the development of the algorithms proposed in Nguyen et al. (2001),Sussman (2003) and Tanguy et al. (2007). More recently, Malan et al. (2021) proposed a different approach for evaporating flows which serves the same purpose as required by the present work, i.e. make incompressible VOF schemes compatible with phase-change flows. All these methods share the common feature that require the solution of at least one additional Poisson equation to make the final extended velocity field divergence free.

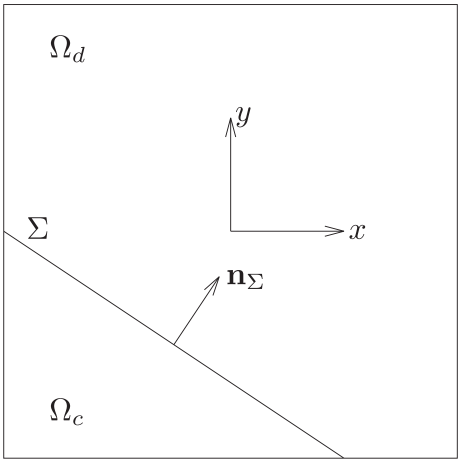

Fig. 2. PLIC reconstruction of a 2D interface.

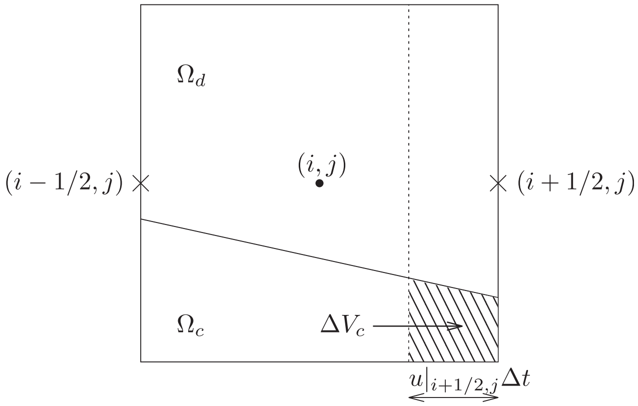

Fig. 3. Geometrical computation of the VOF flux across the cell face $(i+1/2,j)$. ΔV_c is the volume (area in 2D) of liquid transported across the cell boundary.

3.2.2. The velocity extension algorithm

Here we present a novel method to extend the liquid velocity field across the interface and make it divergence free for all the cells which contain liquid ($f>10^{-6}$); the algorithm requires minimum computational effort and it is readily implementable in existing codes. The steps of the algorithm will be illustrated for a 2D problem; extension to 3D is straightforward.

The first step is the computation of the mass transfer rate field ($\dot{m}$) in all the interfacial cells (see Section 3.4); these cells are identified with the criterion $10^{-6}<f<1-10^{-6}$. For each interfacial cell (i,j), the number of pure gas cells which belong to the 3×3 stencil centered on (i,j) is stored in the field $avg|_{i,j}$ (see Fig. 4). These cells are marked as *acceptors* of the *donor* cell (i,j). *Donors* and *acceptors* are clearly related, and a *donor* (*acceptor*) may have multiple *acceptors* (*donors*).

The second step is the redistribution of the mass transfer rate term $\dot{m}$. For each *acceptor*, the contribution from all the relative *donors* is computed and stored in the new field $\dot{m}'$, which is defined only for *acceptors* cells and set to null for the others. The information of the interfacial area A_Σ from the *donors* is also passed to $\dot{m}'$, which is computed as (see Fig. 5):

$$\dot{m}' = \sum_{donors} \frac{\dot{m}}{avg} A_\Sigma \tag{33}$$

Eq. 33 ensures that the overall mass which is exchanged between the phases per time unit is conserved, i.e. $\sum_\Omega \dot{m} A_\Sigma = \sum_\Omega \dot{m}'$. The mass transfer term $\dot{m}$ is finally replaced by the new field $\dot{m}'$ in the projection step of the Navier–Stokes solver, which becomes:

$$\nabla \cdot \left(\frac{\Delta t}{\rho_{n+\frac{1}{2}}} \nabla p \right) = \nabla \cdot \mathbf{u}_* - \dot{m}'_{n+\frac{1}{2}} \left(\frac{1}{\rho_d} - \frac{1}{\rho_c} \right) \frac{1}{V} \tag{34}$$

The new pressure equation ensures that the projected velocity field is divergence free everywhere if $\dot{m}' = 0$ (which is always true in pure liquid and interfacial cells) and provides a natural extension of the continuous phase velocity across the interface. We remark that the terms *acceptor* and *donor* refer to the transfer of the mass source term from the interfacial cells (*donors*) to the neighbouring pure gas cells (*acceptors*), irrespective of the direction of the mass exchange (e.g from liquid to gas or vice versa) and that the redistributed term $\dot{m}'$ is always null in pure liquid and interfacial cells. A drawback of the proposed methodology is given by the possibility that no *acceptors* exist for one or more *donors*. This can happen for highly curved interfaces and/or low mesh resolution; however, the present work aims at direct numerical simulations, where a fine mesh is always required to capture all the flow features and we assume that the grid is fine enough to provide at least one *acceptor* for each *donor*. At this point we remind that the idea of redistributing the mass transfer term has already been proposed in the literature by Hardt and Wondra (2008) and successfully used for diffusion-driven phase change flows (Vachaparambil and Einarsrud, 2020). However, the methodology of Hardt and Wondra (2008) was developed to reduce numerical instabilities which occur when the source term is distributed in a narrow layer of cells and does not provide a divergence free velocity field in all the liquid and mixed cells. Contrary to Hardt and Wondra (2008), our approach does not require the solution of an additional inhomogeneous Helmholtz equation and completely removes the source term from the interfacial cells. We finally remind that the mass transfer term $\dot{m} A_\Sigma$ is substituted by $\dot{m}'$ in Eq. 34 only and is left unchanged in the source terms of the VOF Eq. (30) and Species Transport Eq. (24). It is worth noting that the face-centered velocity field used for the advection of the interface (Eq. 32) is the same as the one used for the advection term of the momentum equation (Section 3.1), making the (convective) transport of momentum consistent with the transport of the interface. The reader is referred to Section 4.2 for the assessment of the momentum conservation property of the proposed methodology.

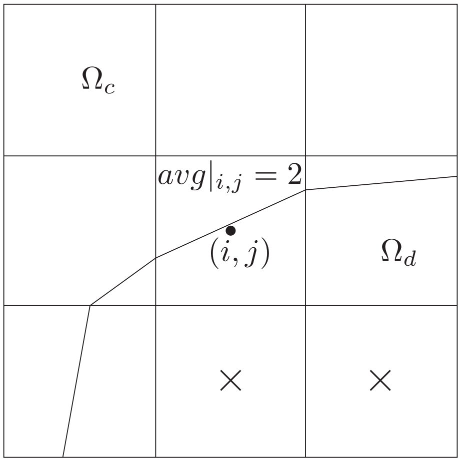

Fig. 4. 2D example of the computation of the field *avg*. The number of *acceptors* (marked with an ×) for the *donor* cell (i,j) is 2.

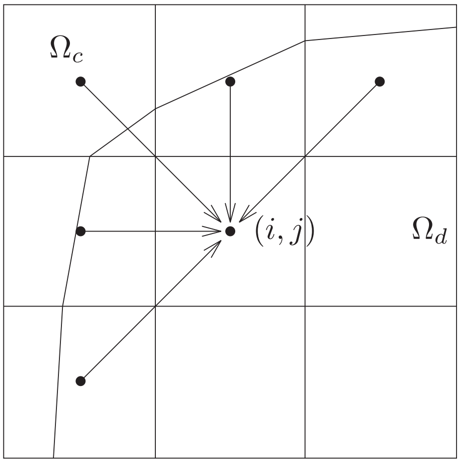

Fig. 5. Computation of $\dot{m}'$. The *acceptor* cell (i,j) receives from each *donor* (five in this example) a contribution equal to $\frac{\dot{m}}{avg} A_\Sigma$.

3.2.3. Step 2. The mass transfer term

The second step is the integration of the mass transfer term:

$$\frac{f_{n+\frac{1}{2}} - f_*}{\Delta t} = -\frac{1}{V} \int_V \frac{\dot{m}}{\rho_c} \delta_\Sigma \, dV \tag{35}$$

Coherently with the PLIC-based approach of the VOF scheme, we follow the same approach of Malan et al. (2021) and integrate Eq. 35 in a geometric way. The contribution of the mass transfer rate consists in a rigid displacement of the interface, along the normal direction $\mathbf{n}_\Sigma$:

$$\mathbf{h} = -\frac{\dot{m}}{\rho_c} \frac{\Delta t}{\Delta} \mathbf{n}_\Sigma \tag{36}$$

where Δ is the mesh size. The equation describing the shape of the interface still has the same form of Eq. 31, with $(\mathbf{n}_\Sigma)_{n+1/2} = (\mathbf{n}_\Sigma)_*$ and:

$$\alpha_{n+\frac{1}{2}} = \alpha_* - \frac{\dot{m}}{\rho_c} \frac{\Delta t}{\Delta} \sqrt{\left[(n_{\Sigma x})^2 + (n_{\Sigma y})^2 + (n_{\Sigma z})^2 \right]_*} \tag{37}$$

The volume fraction $f_{n+1/2}$ is then uniquely determined from $(\mathbf{n}_\Sigma)_{n+1/2}$ and $\alpha_{n+1/2}$. This approach is consistent with the geometric (PLIC) description of the interface and avoids over- and undershoots ($f > 1$ and $f < 0$, respectively) when a cell is completely filled with liquid or gas.

3.3. Species Transport Equation

The integration of the species transport Eq. (23) is a challenging step of the numerical methodology, as the molar concentration profile is generally discontinuous across the interface (Henry's law). A suitable numerical method must be able to preserve such discontinuity and avoid any artificial diffusion of the concentration. The problem is indeed very similar to the advection of the

Heaviside function and this suggests that the choice of the right approach must rely on the method used to transport the volume fraction field (Deising et al., 2016). Since Basilisk adopts a geometric VOF method, we opted for the two-scalar approach (Bothe and Fleckenstein, 2013; Fleckenstein and Bothe, 2015), which has the advantage of applying the same geometric fluxes used for f to the species concentration c, making the advection of c consistent with the displacement of the interface. The two-scalar approach requires the integration of two equations for each species (one for c_c and one for c_d) but, as noted in Section (2.2), in this work we only need to solve for the gas concentration in the liquid phase (c_c). Eq. 23 can then be integrated in the following form:

$$\frac{\phi_{n+\frac{1}{2}}-\phi_{n-\frac{1}{2}}}{\Delta t}+\oint_{\partial V} c\mathbf{u}_c\cdot\mathbf{n}\,dS=\oint_{\partial V} D\nabla c\cdot\mathbf{n}\,dS-\frac{\dot{m}}{M}\frac{A_\Sigma}{V} \tag{38}$$

where the cell-volume average ϕ is related to the phase-average via the following relationship:

$$\phi = f\frac{1}{V_c}\int_{V_c} c\,dV \tag{39}$$

The first step of the numerical integration is the advection term, which is performed with the same split method used for the VOF equation. The scheme is presented in López-Herrera et al. (2015) and the fluxes for each pair of boundaries are computed by multiplying the face value of c (obtained with the unsplit upwind method of Bell et al. (1989)) by the amount of liquid volume ΔV_c which is transported trough the cell face (see Fig. 3). In this way the advection of ϕ is made consistent with the advancement of the interface and any artificial mass transfer is prevented.

After the integration of the mass transfer term (last term on the RHS of Eq. 38), the diffusion step is performed by using the multigrid solver. As for the advection, we need to prevent any transfer of ϕ across the interface at this stage, beacuse the whole mass transfer is given by $\dot{m}$ (which is integrated separately). We use the same approach of (López-Herrera et al., 2015; Magdelaine-Guillot de Suduiraut, 2019) to put the diffusive term in a convenient way for FV discretization schemes, where the variables are averaged over the volume cell (e.g. ϕ) rather than the sub-volume occupied by a specific phase (e.g. c). A 2D example of flux computation for the phase-average concentration c is given below for the control volume shown in Fig. 6:

$$\partial_t c=\frac{D}{V_c}\left[\left(\frac{\partial c}{\partial x}S_c\right)_{i+\frac{1}{2},j}-\left(\frac{\partial c}{\partial x}S_c\right)_{i-\frac{1}{2},j}-\left(\frac{\partial c}{\partial y}S_c\right)_{i,j-\frac{1}{2}}\right] \tag{40}$$

where S_c is the (variable) face area of each boundary of the control volume V_c and the flux across the interface as been set to zero to prevent mass transfer between the phases. Eq. 40 can be easily generalized as:

$$f\partial_t c=\frac{D}{V}\sum_{cellfaces} f_f D\frac{\partial c}{\partial \mathbf{n}}A \tag{41}$$

where the face fraction $f_f = S_c/A$ has been introduced and A is the cell face area. The advantage of formulation 41 is that this equation can be readily solved with standard FV schemes, after the diffusion coefficient is replaced by $f_f D$ and the transient term multiplied by f.

3.4. Mass transfer term

The mass transfer term appears in the continuity Eq. (6), interface Eq. (12) and species transport Eq. (24); it is evident that an accurate solution depends on the discretization scheme used to compute $\dot{m}$. As noted in Section 2.2, the gradient of concentration in the mass transfer term (Eq. 21) must be evaluated in the liquid domain, since the concentration is constant in the disperse phase.

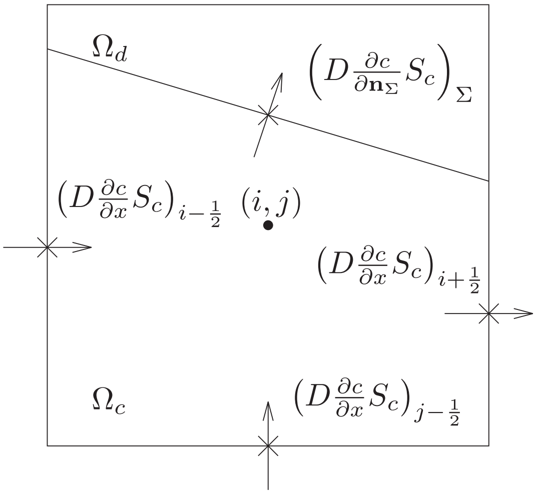

Fig. 6. Flux computation for the diffusion of c in Ω_c. The concentration field must be confined in the liquid region and the flux across the interface is set to $\left(D\frac{\partial c}{\partial \mathbf{n}_\Sigma}S_c\right)_\Sigma = 0$.

Here we use the same unsplit geometric method approach proposed in Bothe and Fleckenstein (2013). The scheme is shown in Fig. 7 for a 2D case. P is the centroid of the interface in the interfacial cell (i,j) and the values of concentration in P_1 and P_2 are obtained from quadratic (bi-quadratic in 3D) interpolation. For points P_1 and P_2, the values used for quadratic interpolation are the closest cell-centered and the values in the top and bottom cells, if $|n_{\Sigma x}| > |n_{\Sigma y}|$, or right and left cells, when $|n_{\Sigma y}| > |n_{\Sigma x}|$. The gradient is then computed by weighting the two first-order derivatives:

$$-\frac{\partial c}{\partial \mathbf{n}_\Sigma}=f\frac{c(P_1)-c(P)}{\overline{PP_1}}+(1-f)\frac{c(P_2)-c(P)}{\overline{PP_2}} \tag{42}$$

where the concentration in P is given by Henry's law, i.e. $c(P) = c_d/He$. The grid convergence order of this numerical scheme is tested for the 1D concentration profile shown in Fig. 8 (left). This profile is the solution to the Stefan problem for a planar interface (see Section 4.3 for details) and is given by the following formula:

$$c(x,t)=c_\Sigma\left(1-erf\left(\frac{x-x_\Sigma(t)}{2\sqrt{Dt}}\right)\right)\quad \text{for } x>x_\Sigma \tag{43}$$

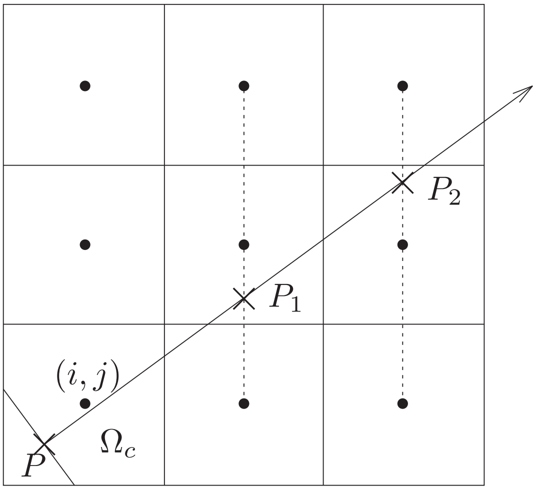

Fig. 7. Concentration gradient scheme (2D). The concentrations in P_1 and P_2 are obtained by quadratic interpolation from the neighbouring values.

where x_Σ and D are the position of the interface and the diffusivity of the gaseous species, respectively. The gradient of the concentration at the interface is:

$$\left(\frac{\partial c}{\partial x}\right)_{x=x_\Sigma} = -\frac{c_\Sigma}{\sqrt{\pi D t}} \tag{44}$$

The numerical derivative (Eq. 42) is computed for five different grids with decreasing mesh size (Δ) and compared against the analytical solution (Eq. 44). The error is computed as:

$$Err = \left| \frac{\left(\frac{\partial c}{\partial x}\right)^a_{x=x_\Sigma} - \left(\frac{\partial c}{\partial x}\right)^n_{x=x_\Sigma}}{\left(\frac{\partial c}{\partial x}\right)^a_{x=x_\Sigma}} \right| \tag{45}$$

where the superscripts a and n refer to the analytical and numerical solutions respectively; results are reported in Fig. 8 (right) and show that the numerical method converges with second order accuracy.

4. Validation

In this Section, the proposed methodology is validated against several benchmark tests which have analytical or semi-analytical solutions. Our numerical approach consists of two main parts which need to be tested, i.e. the velocity extension algorithm (Section 3.2.2) and the gradient scheme used to compute $\dot{m}$ (Section 3.4). The first test case is aimed at validating the correctness of the velocity extension algorithm and consists of a growing/shrinking bubble with a constant mass transfer rate (Section 4.2). The classic benchmark for phase-change schemes - the Stefan problem - is presented in Section 4.3, while the solution for bubbles immersed in a super-saturated and under-saturated solutions is shown in Sections 4.4.1 and 4.4.2 respectively. The last two validation benchmarks consider the case of moving bubbles: the problem of a dissolving bubble rising in a low-Reynolds flow is presented in Section 4.5, while a quantitative analysis of the mesh refinement needed to capture the concentration boundary layer is shown in Section 4.6 for rising bubbles at different Péclet numbers.

The governing equations are solved in their non-dimensional form and the relevant non-dimensional numbers are introduced in Section 4.1. We remind that we refer to the gaseous (liquid) phase as the disperse (continuous) phase and that these terms can be used interchangeably in the following; the concentration in the gaseous phase is assumed to be constant as no mixtures of species are considered in the present work.

4.1. Non-dimensional groups

The dynamics of a bubble in a gravitational field can be described by the Galilei and Bond numbers. The Galilei number compares the gravitational and viscous forces and is defined as:

$$Ga^2 = \frac{g D_b^3}{\nu_c^2} \tag{46}$$

where D_b is the bubble diameter and ν_c is the kinematic viscosity of the continuous phase. The ratio of gravitational and capillary forces is estimated by the Bond number:

$$Bo = \frac{\rho_c g D_b^2}{\sigma} \tag{47}$$

For rising bubbles, the Reynolds number is defined as:

$$Re = \frac{\rho_c U_b D_b}{\mu_c} \tag{48}$$

where U_b is the velocity magnitude of the gravitational center of the bubble.

When mass transfer driven by species diffusion occurs, the Schmidt number compares momentum diffusion to mass diffusion:

$$Sc = \frac{\nu_c}{D_c} \tag{49}$$

The ratio between the advection-driven transport of a species to the diffusive transport of the same species is given by the Péclet number:

$$Pe = ReSc \tag{50}$$

For applications involving mass transfer phenomena, it is useful to introduce the Sherwood number:

$$Sh = \frac{k_l L_{ref}}{D_c} \tag{51}$$

where k_l is the mass transfer coefficient given by:

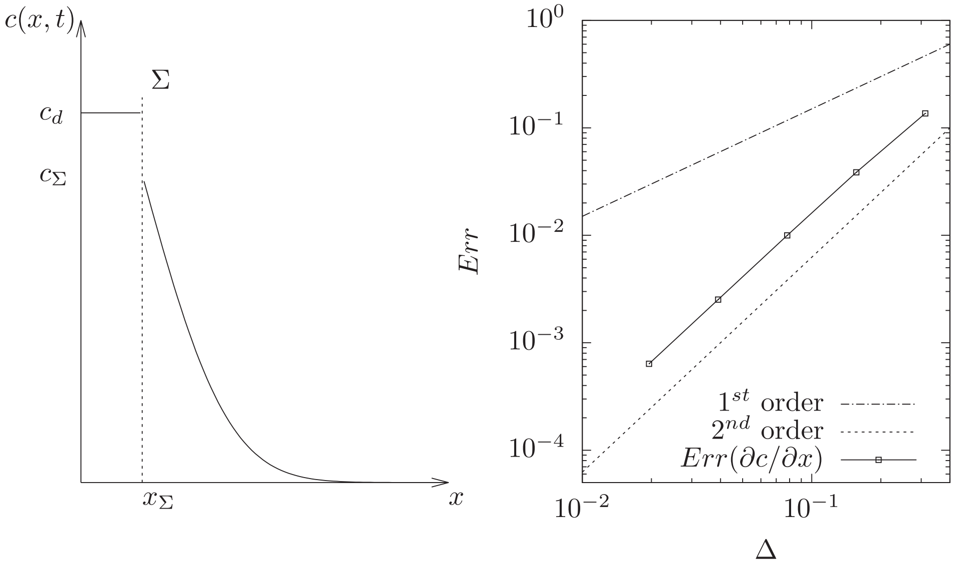

Fig. 8. 1D concentration profile (left) and grid convergence analysis (right). The discontinuity across the interface in the concentration profile is given by Henry's Law ($c_\Sigma = c_d/He$). The non-dimensional time and gas diffusivity are $t = 0.8$ and $D = 0.19$.

$$k_l = \frac{\int_\Sigma \dot{m}\, dS}{A_\Sigma M (c_\Sigma - c_{bulk})} \tag{52}$$

A_Σ is the area of the interface, M the molar mass of the transferred species and c_{bulk} is the species concentration in the bulk liquid.

The amount of chemical species which is initially dissolved in the liquid is a technical parameter which can be controlled in experiments and the *saturation ratio* compares the bulk liquid concentration and the interface concentration at equilibrium (saturated interface):

$$\zeta = \frac{c_{bulk}}{c_\Sigma} \tag{53}$$

Depending on the value of ζ, three different scenarios can occur: saturated solution ($\zeta = 1$), under-saturated solution ($\zeta < 1$) and super-saturated solution ($\zeta > 1$). When $\zeta > 1$, an excess of species is dissolved in the liquid and diffusion will transfer gas from the continuous phase to the disperse one (growing bubble) in order to recover the equilibrium solution ($\zeta = 1$). For the same reason, bubbles will shrink when $\zeta < 1$.

If it is not specified, we assume the bubble diameter as the reference length (L_{ref}) for the non-dimensional coordinates ($\mathbf{x}/L_{ref}$), while the reference time is given for each problem in the following sections.

4.2. Bubble with a fixed mass transfer rate

In this test we model a single 3D spherical bubble with constant mass transfer rate. The accuracy of the solution depends on the correctness of the velocity extension algorithm, which can be tested properly here, since $\dot{m}$ is known (and, therefore, no additional discretization errors are introduced). The properties of the gas–liquid system are the same as for CO_2 - water and are reported in Table 1. The initial bubble diameter is $D_b = 0.01$ m, the reference time is $t_{ref} = \rho_c D_b^2/\mu_c$ and the mass transfer rate is $\dot{m} = \pm 1.8 \times 10^{-2}$ kg/m^{2}s. The computational domain is a cube with dimension $L0 = 50 D_b$ and the finest mesh size is $\Delta = L0/2^{11}$ ($LEVEL = 11$), which corresponds to approximately 40 cells per diameter. We use the AMR technique to keep the mesh at the maximum refinement level around the interface, while a coarser grid is distributed far from the bubble. Gravity is neglected and outflow boundary conditions (fixed pressure and zero gradient for the velocity) are assigned to all the external boundaries. For this test case, the analytical solution for the time-evolving radius is given by:

$$R(t) = R(0) + \frac{\dot{m}}{\rho_d} t \tag{54}$$

Fig. 9 (left) compares the analytical solution (Eq. 54) against two numerical results, obtained with and without the velocity extension algorithm. It is evident that the solution without velocity extension completely misses the movement of the interface, as a result of the non-solenoidal velocity field in interfacial cells (which produces strong pressure/velocity fluctuations around the interface). On the other hand, the numerical solution obtained by applying the velocity extension algorithm is able to capture the correct solution. A small deviation from the analytical solution is observed for $t/t_{ref} > 0.04$, where the mesh is not fine enough to capture the flow features. Fig. 10 shows the velocity field around the interface (left) and the corresponding divergence field (right). The velocity field is axisymmetric and preserves the spherical shape of the bubble; the divergence field obtained from the redistribution of the mass transfer term is null everywhere both in the bulk liquid and interfacial cells. The purpose of the velocity extension algorithm (Section 3.2.2) is therefore achieved and the velocity field is not divergence-free only in the first row of pure gas cells next to the interface; vectors show that the resulting liquid velocity field is smoothly extended across the interface. A similar test case is shown in Fig. 9 (right) for a growing bubble with $\dot{m} = 1.8 \times 10^{-2}$ kg/m^{2}s. In this case the mesh refinement is always sufficient to resolve the interface and the numerical solution is accurate at every time step. The consistency between the transport of the interface and momentum is shown in Fig. 11 for the growing bubble case. As the bubble grows, a certain amount of liquid ($dm(t)$) crosses the boundaries and leaves the numerical domain. This quantity can be evaluated both from the boundary fluxes of momentum as:

Table 1
Gas–Liquid properties.

Phase	Density $\left[\frac{kg}{m^3}\right]$	Viscosity $\left[\frac{Ns}{m^2}\right]$	Surface tension $\left[\frac{N}{m}\right]$
Liquid	1000	1.05×10^{-3}	0.072
Gas	1.8	1.46×10^{-5}	

$$dm\left(t_{n+\frac{1}{2}}\right)^{Flux} = \Delta t \int_{\partial\Omega} \rho_c |\mathbf{u} \cdot \mathbf{n}|\, dS \tag{55}$$

and from the Volume of Fluid field as:

$$dm\left(t_{n+\frac{1}{2}}\right)^{VOF} = \left| \int_\Omega f_* \rho_c\, dV - \int_\Omega f_{n-\frac{1}{2}} \rho_c\, dV \right| \tag{56}$$

where f_* is the VOF field at $t_{n+\frac{1}{2}}$ right after the advection step, but before the phase-change term is applied. The imbalance between $dm\left(t_{n+\frac{1}{2}}\right)^{Flux}$ and $dm\left(t_{n+\frac{1}{2}}\right)^{VOF}$ is monitored during the simulation and the relative error decreases constantly and approaches a value below 0.01% (Fig. 11).

These tests show that extending the liquid velocity field across the gas–liquid interface is a crucial step for the advection of the interface and that the proposed methodology gives accurate predictions.

4.3. Stefan problem

The Stefan problem is a classic benchmark for phase-change schemes and consists in a planar interface which separates the gas and liquid regions. The diffusion of gas into the liquid activates the fluid flow and drives the displacement of the interface. The liquid is initially under-saturated ($\zeta = 0$) and no gravity and surface tension are taken into account. The properties of the system are the same as reported in Table 1 and two different gas diffusivities are tested: $D = 2 \times 10^{-9}$ m^2/s and $D = 2 \times 10^{-7}$ m^2/s. The first case corresponds to the diffusion of CO_2 in water and the relative Schmidt number is $Sc = 526$, while the large diffusion case has $Sc = 5.26$; Henry's coefficient is set to $He = 1.203$ for both tests. The reference length is $L_{ref} = 0.01$ m and the computational domain is a square of length $L0 = L_{ref}$ for $Sc = 526$ and $L0 = 10 L_{ref}$ for $Sc = 5.26$. The interface is a horizontal line and the liquid region is on top of it; an outflow boundary condition is applied at the top boundary, while symmetric conditions are set for the other boundaries. The reference time is $t_{ref} = \rho_c L_{ref}^2/\mu_c$, whilst the species concentration is nondimensionalized with the pure gas concentration, which is a material property of the gas (see Section 2.2). A qualitative representation of the problem is given in Fig. 12 for the case $Sc = 5.26$.

For this problem, the exact solution can be found analytically (Crank, 1975) and is characterized by a null velocity field in the gas region, while the liquid velocity is given by:

$$|\mathbf{u}_c| = \frac{\rho_c - \rho_d}{\rho_c} |\mathbf{u}_\Sigma| \tag{57}$$

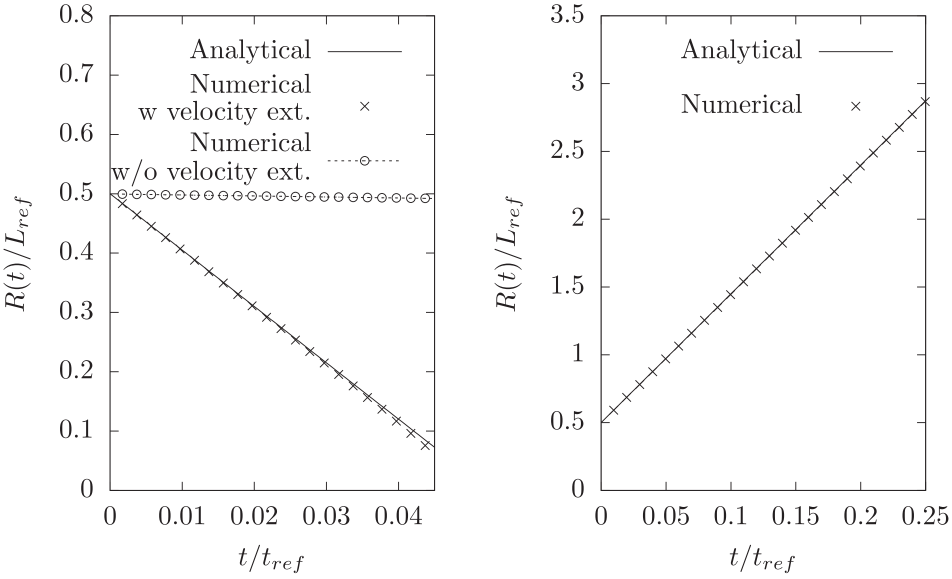

Fig. 9. Radius evolution for a suspended bubble with constant mass transfer rates $\dot{m} = -1.8 \times 10^{-2}$ kg/m^{2}s (left) and $\dot{m} = 1.8 \times 10^{-2}$ kg/m^{2}s (right).

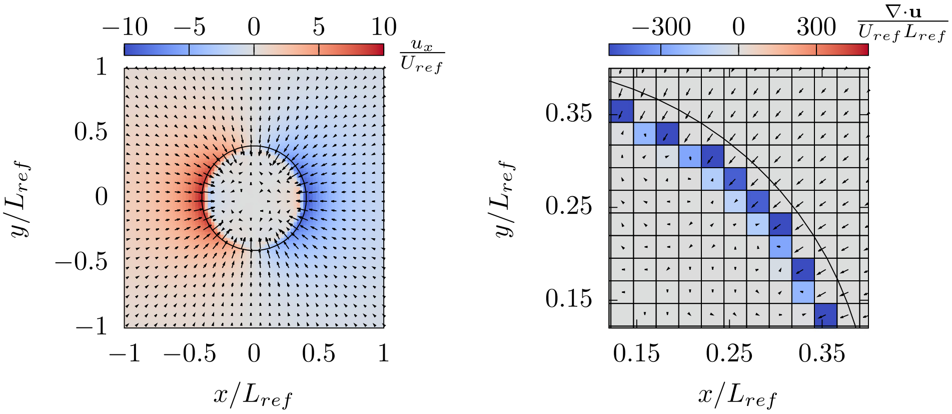

Fig. 10. Velocity field and contours of horizontal velocity (left) and velocity divergence field (right) for a collapsing bubble with $\dot{m} = -1.8 \times 10^{-2}$ kg/m^{2}s. Snapshot taken at $t/t_{ref} = 0.01$.

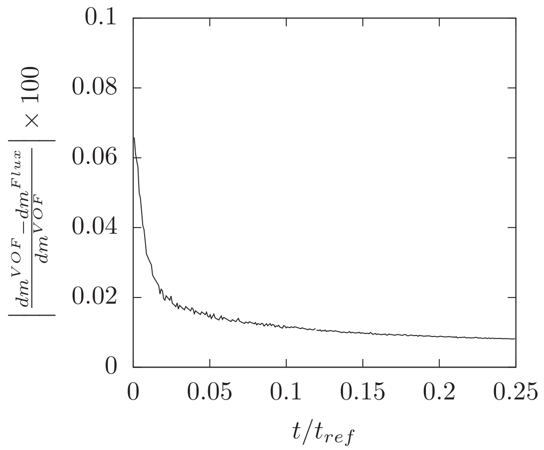

Fig. 11. Relative error of the imbalance between the amount of liquid that crosses the external boundaries based on the fluxes of momentum (dm^{Flux}) and VOF field (dm^{VOF}), for the growing bubble case.

The interface velocity magnitude is:

$$|\mathbf{u}_\Sigma| = \frac{D}{He\sqrt{\pi D t}} \tag{58}$$

and the interface displacement can be found by integrating Eq. 58:

$$l(t) = \frac{2}{He}\sqrt{\frac{tD}{\pi}} \tag{59}$$

Finally, the species concentration in the liquid region is:

$$c(y,t) = c_\Sigma\left(1 - erf\left(\frac{y - y_\Sigma(t)}{2\sqrt{Dt}}\right)\right) \tag{60}$$

A grid convergence study is performed for the large diffusivity case ($Sc = 5.26$). Results are reported in Fig. 13 and show the error convergence for both the interface displacement and amount of gas moles dissolved in the liquid (left) and the plot of the time evolving interface displacement (right). Five grids are tested and each grid is identified by the hierarchical level of the respective finest cell in the quadtree structure. The mesh size for each level is $\Delta = L0/2^{LEVEL}$, where $L0$ is the domain length ($L0/L_{ref} = 10$, for this case). The

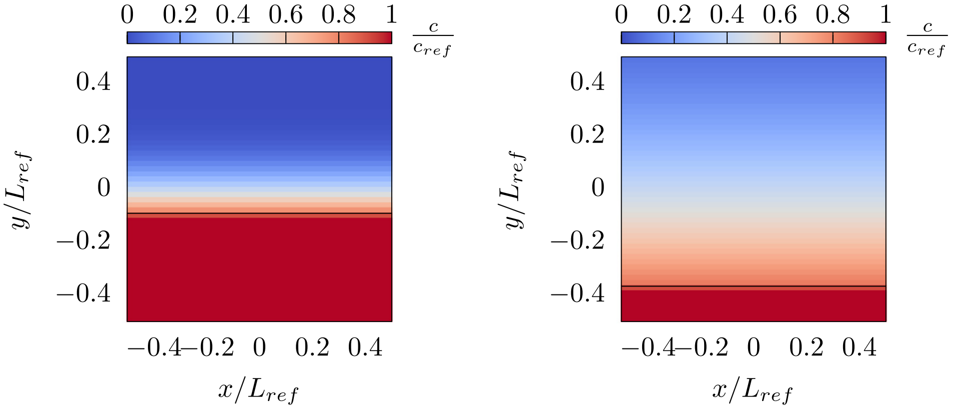

Fig. 12. Interface displacement and contour of species concentration ($Sc = 5.26$) at $t/t_{ref} = 0.05$ (left) and $t/t_{ref} = 0.8$ (right).

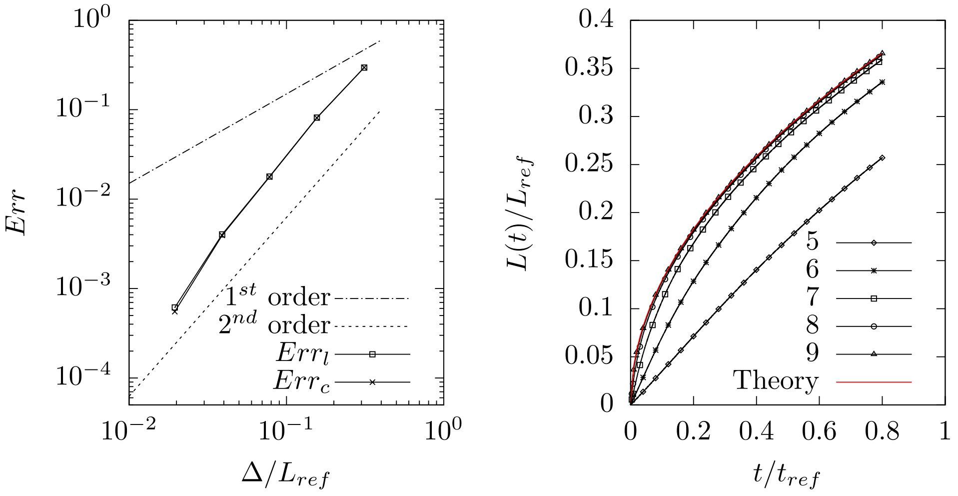

Fig. 13. Grid convergence study (left) and interface displacement (right) with five different resolutions for the Stefan problem with $Sc = 5.26$ at $t/t_{ref} = 0.8$.

errors on the interface (Err_l) and on the dissolved gas moles (Err_c) are computed as:

$$Err_l(\Delta, t) = \left|\frac{l_a(t) - l_n(\Delta, t)}{l_a}\right| \tag{61}$$

and

$$Err_c(\Delta, t) = \left|\frac{\int_{\Omega_c} c_a(y,t)\,dV - \int_{\Omega_c} c_n(y,t)\,dV}{\int_{\Omega_c} c_a(y,t)\,dV}\right| \tag{62}$$

where the subscripts a and n refer to the analytical and numerical solutions respectively. For both quantities, the convergence of the solution is close to second order, coherently with the accuracy of the scheme used for the gradient of species concentration (see Section 3.4). For the finest grid ($LEVEL = 9$), the mesh size is $\Delta/L_{ref} \approx 0.0195$ and the relative error on the interface position at $t/t_{ref} = 0.8$ is approximately 0.06%. For the low diffusivity case ($Sc = 526$), a thinner concentration boundary layer is obtained and a finer mesh with $\Delta/L_{ref} \approx 0.0039$ is used. The interface displacement is plotted in Fig. 14 for both cases and compared with the analytical solution. In both configurations, the numerical solution provides an accurate prediction of the interface location. Velocity and concentration profiles along the vertical line $y = 0$ are plotted in Fig. 15 and compared against their respective analytical solutions (Eqs. 57 and 60). Both types of profiles are characterized by discontinuities across the interface which are accurately captured by our numerical simulations. The velocity profile at $t/t_{ref} = 0.05$ shows a small deviation from the expected results; such behaviour is probably due to the initialization of the simulation which assumes that the interface is saturated while no gas is yet dissolved into the liquid. Such nonphysical initial condition is then adsorbed as soon as a diffusion boundary layer develops around the interface, and no significant deviations are reported for velocity profiles at later times.

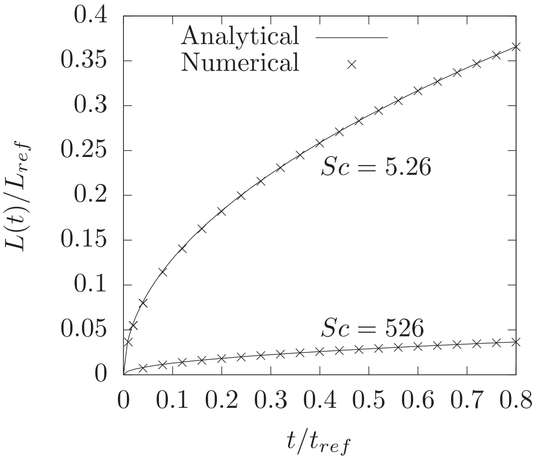

Fig. 14. Interface displacement for the Stefan problem.

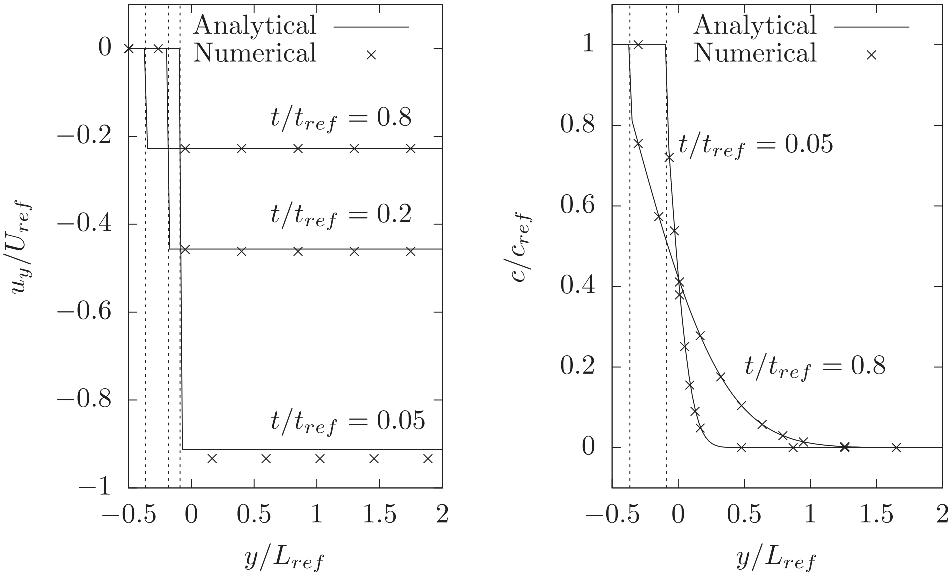

Fig. 15. Velocity (left) and concentration (right) profiles along the line $y = 0$ at different times for the Stefan problem with $Sc = 5.26$. The dotted lines show the interface locations.

4.4. Suspended bubbles

In this section we study the mass transfer of gas from bubbles suspended in a liquid solution. Since no gravity is taken into account, the center of the bubble is fixed. We consider both cases of growing (Section 4.4.1) and dissolving (Section 4.4.2) bubbles. The properties of the gas–liquid system are the same as reported in Table 1. Henry's coefficient is $He = 5$, while the diffusivity of gas in liquid is set to $D = 2 \times 10^{-5}$ m^2/s which corresponds to $Sc = 0.0526$. Such increase in the diffusion coefficient with respect to typical values for gas diffusivities in liquids ($D \approx 10^{-9}$ m^2/s) leads to a reduction of computational cost, since the resulting mass transfer rate is speeded up ($\dot{m} \propto D$). The reference time is set to $t_{ref} = \rho_c D_b^2 / \mu_c$ in both cases.

4.4.1. Bubble growing in a super-saturated solution

In this section we model a single 3D spherical bubble immersed in a supersaturated solution ($\zeta > 1$) with a constant initial concentration. The analytical solution for this problem was found by Scriven (Scriven, 1959) and the resulting equation for the radius of the bubble is:

$$R(t) = 2\beta\sqrt{Dt} \tag{63}$$

The non-dimensional factor β depends on the gas and liquid densities (ρ_d, ρ_c), initial bulk concentration in liquid (c_{bulk}) and interfacial concentration (c_Σ):

$$\Phi = 2\beta^3 \exp\left(\beta^2 + 2\epsilon\beta^2\right) \int_\beta^\infty x^{-2} \exp\left(-x^2 - 2\epsilon\beta^3 x^{-1}\right) dx \tag{64}$$

where

$$\Phi = \frac{\rho_c}{\rho_d} \frac{M(c_{bulk} - c_\Sigma)}{\rho_c - M c_\Sigma} \tag{65}$$

and

$$\epsilon = \frac{\rho_c - \rho_d}{\rho_c} \tag{66}$$

The bubble initial diameter is $D_b = 0.01$ m and the computational domain is a cube with dimension $L0 = 50D_b$; outflow boundary conditions are applied to all the external boundaries. Eq. 63 assumes that no bubble exists at $t = 0$ (i.e. $R(0) = 0$); however, within the VOF approach, the volume fraction of gas must be initialized (i.e. a bubble must be generated). In order to make the numerical results comparable with the analytical solution, we first initialize the solution with a constant bubble size ($R = 0.005$ m) where $\dot{m}$ is taken into account in the species transport equation only. This allows a realistic concentration field around the bubble to be obtained at $t = \bar{t}$, where $\bar{t}$ is the time required for the radius to grow to $R(\bar{t}) = 0.005$ m, according to Eq. 63. For $t > \bar{t}$ the full phase-change model is solved and the bubble volume is free to evolve. A summary of the cases simulated here is reported in Table 2.

A mesh sensitivity study is performed for the case $\zeta = 2$. Four different grids are tested and the relative error on the radius prediction at $t/t_{ref} = 0.3$ is reported in Table 3. The number of cells per diameter reported in Table 3 refers to the initial bubble diameter. The mesh with $LEVEL = 10$ is a good compromise between accuracy and computational cost and the same grid is used for the other cases reported in this section.

A qualitative representation of the problem is given in the slices reported in Fig. 16, for the case $\zeta = 2$. Two snapshots taken at different times are compared and the figure clearly shows the evolution of the concentration boundary layer around the gas–liquid interface as the bubble grows.

Results of the time-evolving radius are compared in Fig. 17 against the theoretical solution. For all the saturation ratios tested here, the numerical methodology provides accurate predictions.

4.4.2. Bubble dissolving in an under-saturated solution

In this section, we study the dissolution of a bubble in an under-saturated solution with no initial concentration of gas ($\zeta = 0$). The numerical setup is similar to that used for the growing bubble cases (Section 4.4.1); the domain size is reduced to $L0 = 20D_b$

Table 2
Summary of test cases for a growing bubble in a super-saturated solution.

ζ	β	$\bar{t}/t_{ref}$
2	0.421	0.0186
3	0.669	0.0073
4	0.895	0.0041

Table 3
Relative errors on radius at $t/t_{ref} = 0.3$ for the case $\zeta = 2$.

LEVEL	#cells/D_b	Error %
8	≈ 5	8.34
9	≈ 10	2.56
10	≈ 20	1.2
11	≈ 41	0.89

and a finer mesh with approximately 102 points per diameter is used. This choice is justified by the fact that more cells are needed to properly resolve the flow around the interface as the bubble dissolves. The simplified problem which neglects the advection term in the species transport equation:

$$\begin{aligned} &\partial_t c = \nabla \cdot (D \nabla c) \\ &c(r,0) = c_{bulk} \quad \text{for} \quad r > R \\ &c(R,t) = c_\Sigma \quad \text{for} \quad t > 0 \\ &\lim_{r \to \infty} c(r,t) = c_{bulk} \quad \text{for} \quad t > 0 \end{aligned} \tag{67}$$

was solved analytically by Epstein and Plesset (Epstein and Plesset, 1950) for a domain internally bounded by a sphere with a constant radius R. The solution to Eq. 67 can be used to approximate the case of a bubble exchanging mass with the surrounding liquid (where R is time dependent). Such a quasi-stationary approximation is as accurate as the mass transfer process is slow (i.e. the effect of the liquid velocity is negligible compared to diffusion) and the growth of the concentration boundary layer is fast compared to the rate of dissolution (Duda and Vrentas, 1971). This is usually the case for gas bubbles dissolving in liquids, since diffusion coefficients are typically small. The solution in terms of bubble radius is:

$$\frac{dR}{dt} = \frac{DM(c_{bulk} - c_\Sigma)}{\rho_d}\left[\frac{1}{R} + \frac{1}{\sqrt{\pi D t}}\right] \tag{68}$$

and the concentration field is given by (Crank, 1975):

$$c = c_{bulk} + (c_\Sigma - c_{bulk})\frac{R}{r}\operatorname{erfc}\left(\frac{r-R}{2\sqrt{Dt}}\right) \tag{69}$$

where c_{bulk} is assumed null for the cases presented in this section.

The accuracy of our numerical methodology is first tested against the exact solution of the Epstein-Plesset (EP) model (Eqs. 68,69), i.e. for a bubble with constant size. In this test, the volume of the bubble is kept fixed and $\dot{m}$ appears as a source term in the species transport equation only. The equivalent time-evolving volume is computed by integrating the mass flux over the bubble surface:

$$V(t) = V(0) + \frac{1}{\rho_d}\int_0^t \oint_\Sigma \dot{m}\, ds\, dt\prime \tag{70}$$

The comparison in terms of radius and concentration profiles between the numerical simulation and the EP model is shown in Fig. 18, where excellent agreement is found.

In the following test case, the full phase-change model is applied and the volume of the bubble changes in time. An approximate analytical solution is given by the EP model, where R is replaced by $R(t)$ in Eq. 68. Since the EP model neglects the advection of the concentration, a significant deviation from the analytical model can be expected when the full species transport equation is solved. Here we present two numerical tests: in the first one we solve the full governing equations, while in the second one we switch off the advection term in the transport of species concentration. Results in terms of radius evolution over time are presented in Fig. 19. As expected, the full numerical simulation deviates significantly from the EP model, as a result of the influence of the convective transport of gas concentration. On the other hand, the second numerical test (without the advection term), matches the EP model with good accuracy until $t/t_{ref} \approx 0.015$, when the dissolution rate becomes too fast for the quasi-stationary approximation. A detailed experimental study on the validity of the EP model can be found in Duncan and Needham (2004). The authors show that the dissolution time of a bubble in an under-saturated solution is generally overpredicted by 8.2% by the EP model with respect to their experimental measurements. However, the dissolution time computed with the EP model was obtained with a simplified version of the model, which neglects the second term on the RHS of Eq. 68 and reads:

$$t_d^{simp} = \frac{\rho_d R^2(0)}{2 D c_\Sigma M (1 - \zeta)} \tag{71}$$

For an air–water system, the full EP model predicts a dissolution time $t_d^{full} \approx 0.84 t_d^{simp}$ (see Epstein and Plesset, 1950) and the conclusions of Duncan and Needham (2004) can be reformulated, stating that the EP model underpredicts the dissolution time by $\approx 10\%$. This correction factor is used in Fig. 19 to plot a corrected curve for the EP model which shows better agreement with the full numerical model, in agreement with the experimental findings.

4.5. Rising bubble in a low-Reynolds flow

In the cases considered so far the bubbles were stationary as neither gravity nor external forces were applied. The aim of this test is to validate our phase-change model for a moving bubble which exchanges mass with the surrounding under-saturated

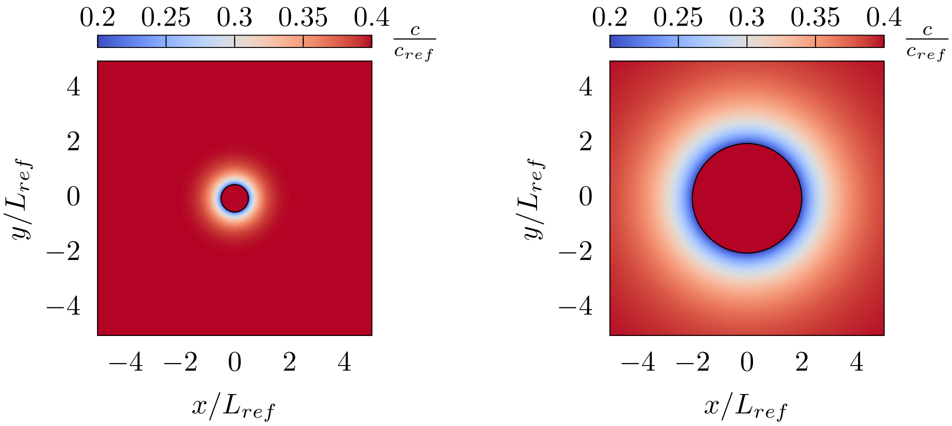

Fig. 16. Interface and contour of species concentration on the XY plane at $t/t_{ref} = 0.01$ (left) and $t/t_{ref} = 0.3$ (right) for the case $\zeta = 2$.

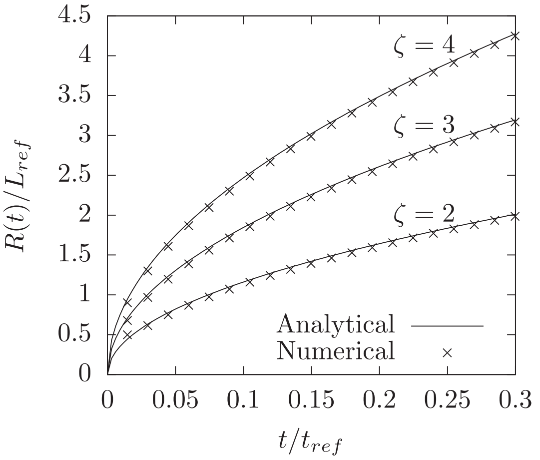

Fig. 17. Time-evolving radius for a growing bubble in super-saturated solutions at different saturation ratios.

liquid ($\zeta = 0$). Here we replicate the same setup proposed in Fleckenstein and Bothe (2015), where the authors derived a semi-analytical solution for a bubble rising with a low speed (creeping flow). The initial bubble diameter is $D_b = 0.004$ m and the computational domain is a cube with dimension $L0 = 120D_b$. The mesh LEVEL is 13 (approximately 68 cells/D_b) and an outflow boundary condition is set on the top face, while symmetric conditions are applied to the other boundaries. The properties of the gas–liquid system are reported in Table 4.

The analytical model of Fleckenstein and Bothe (2015) is based on the Hadamard-Rybczynski solution for the steady-state velocity field around a rigid spherical particle rising in a creeping flow (Hadamard, 1911; Rybczynski, 1911) and the terminal velocity of a particle with radius R is given by:

$$U_b = \frac{2}{3}\frac{\rho_c - \rho_d}{\mu_c} g R^2 \frac{1 + \mu_d/\mu_c}{2 + 3\mu_d/\mu_c} \tag{72}$$

The steady-state velocity obtained by Fleckenstein and Bothe (2015) from their numerical simulation (for a bubble with constant size) is $U_b = 0.03$ m/s, which underestimates the theoretical value predicted by Eq. 72 for the properties reported in Table 4 ($U_b = 0.035$ m/s). Here, in order to validate our model against the same results reported in Fleckenstein and Bothe (2015), we adjusted the gravitational acceleration to $g = 8.92$ m^2/s which ensures that the bubble reaches the same terminal velocity $U_b = 0.03$ m/s. The non-dimensional groups which describe the problem are: $Bo = 2.96, Ga = 2.04$ and $Sc = 250$; the reference time is set to $t_{ref} = \sqrt{D_b/g}$. For these parameters (Bo and Ga) the bubble retains its spherical shape and follows a rectilinear path (Tripathi et al., 2015); the assumptions of the Hadamard-Rybczynski model are then valid for this specific problem. In order to compare our numerical solution against the semi-analytical model, we first need to reach a steady-state solution in terms of rising velocity and concentration field. The simulation is first run without taking into account the volume change related to the mass transfer until the bubble reaches its terminal velocity. During this stage, the species transport equation is solved and the concentration field around the interface evolves until it becomes locally (in a region around the bubble) time-independent (in a reference frame moving with the bubble). After the bubble reaches the steady-state regime, the full phase-change model is applied and the volume starts to shrink as the gas is released into the liquid. In our simulation we reach the bubble terminal velocity at $t_{steady}/t_{ref} \approx 25$ and the results in terms of volume ratio for $t > t_{steady}$ are reported in Fig. 20. The numerical solution shows good accuracy and the relative error on the volume ratio at the end of the simulation (after a physical simulated time of $\Delta t = 0.25$ s) is 0.43%.

A qualitative representation of the problem is shown in Fig. 21, for three different times. The first two pictures show the bubble at time $t/t_{ref} = 0$ and $t/t_{ref} = 20$; the volume is kept constant at this stage, but the concentration field develops as part of the gas is released into the liquid. The last snapshot is taken at time $t/t_{ref} = 40$ and shows the reduction in volume of the bubble. The thickness of the concentration boundary layer is not constant around the interface and depends on which transport mechanism prevails locally. On top of the bubble, the velocity boundary layer is attached to the interface and the concentration profile is constrained into a thin region where diffusion is dominated by convection. Diffusion becomes progressively more relevant as we move along the interface towards the rear part of the bubble, where the concentration boundary layer grows accordingly. The wake

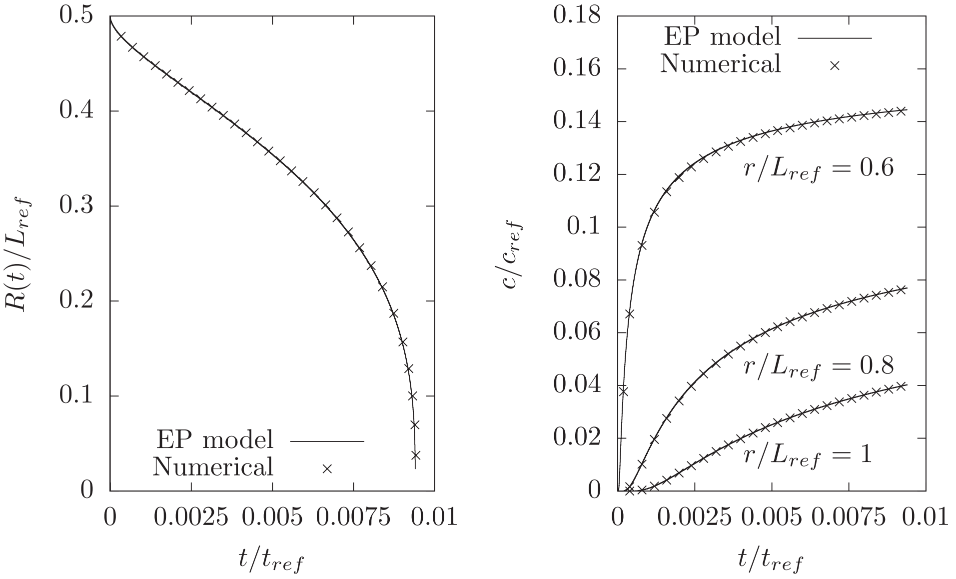

Fig. 18. Comparison between the EP model and numerical simulations of a bubble with constant size: radius (left) and concentration profiles at three different locations (right).

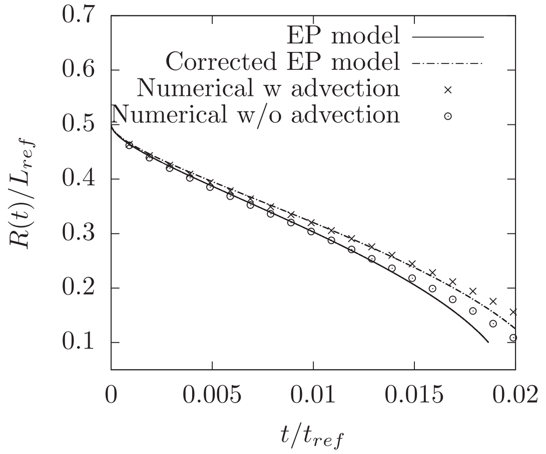

Fig. 19. Time evolving radius for a dissolving bubble. Numerical simulation with and without the advection term are compared and a corrected version of the EP model (based on experimental findings) is plotted.

region close to the bottom of the bubble is characterized by a stagnation velocity field, where diffusion prevails over convection and makes the concentration field almost uniform.

One of the advantages of numerical modelling is that simulations give access to local information that is difficult to obtain experimentally. One example is shown in Fig. 22, where the contour of the mass transfer is plotted on the XZ plane. The mass transfer is a local interfacial property which depends on the concentration gradient (Eq. 21) and is directly related to the thickness of the boundary layer. Fig. 22 shows that the maximum of $\dot{m}$ is on top of the bubble, where the concentration profile is thin and the gradient is steep. The mass transfer progressively decreases as we move towards the rear of the bubble and becomes almost null in the stagnation region where the concentration is constant ($\partial c/\partial \mathbf{n}_\Sigma \approx 0$).

4.6. Rising bubbles at different Péclet numbers

The limiting factor for direct numerical simulations of diffusion-driven mass transfer problems is mainly given by the thickness of the concentration boundary layer δ_c. In order to capture the mass transfer rate at the interface with the numerical scheme given by Eq. 42, the concentration boundary layer must be resolved and enough points must lie within it. Indications on the thickness of δ_c can be obtained from the Péclet number (Eq. 50), i.e. the ratio of convective transport to diffusive transport of species, and the larger is Pe the thinner is the concentration boundary layer. In this section we provide a quantitative analysis of the mesh refinement needed to properly model the mass transfer for rising bubbles at different Péclet numbers. The numerical setup is similar to Section 4.5, but 2D (axisymmetric) bubbles are modelled instead of 3D ones; the rising trajectory is the horizontal x- direction. Only the mass transfer process is computed (i.e. release of gas into the liquid as bubbles rise) and no volume change is taken into account. Three different gas species are modelled that have different diffusivities (D) and, therefore, different Pe numbers. The properties of the gas–liquid systems are reported in Table 5. The bubble diameter is $D_b = 0.001$m and the relative Bond and Galilei numbers are $Bo = 0.163$ and $Ga = 19.77$. The steady-state Re number is the same for all the configurations ($Re \approx 18.6$) since no volume effect is taken into account here; Henry's constant is set to $He = 5$. The Sherwood numbers are compared for the three bubbles against the formula proposed by Takemura and Yabe (1998) (valid for $Re < 100$ and $Pe > 1$):

$$Sh = \frac{2}{\sqrt{\pi}}\left[1 - \frac{2}{3}\frac{1}{\left(1 + 0.09Re^{2/3}\right)^{3/4}}\right]^{1/2}\left(2.5 + \sqrt{Pe}\right) \tag{73}$$

Results are shown in Fig. 23 and for all the cases considered here the numerical solutions approach the values predicted by Takemura and Yabe (1998) as bubbles reach a steady-state rising regime (i.e. constant rising velocity), with a relative error on Sh below 2%. The level of grid refinement needed to achieve a mesh independent solution increases with the Péclet number. The grid sizes (Δ) along with the number of cells per diameter used for these simulations are reported in Table 6. A qualitative representation of the distribution of gas concentration around the interface and the grid refinement needed to resolve the boundary layer is shown in Fig. 24. From the data collected in Table 6 and the contour of Fig. 24 it is clear how strong the Pe number and thickness δ_c are related and how they constrain the mesh resolution around the interface. The concentration profiles at the equator of the bubble (i.e. at $\Theta = \pi/2$, where Θ is the polar coordinate which is $\Theta = 0$ at the leading edge and $\Theta = \pi$ at the trailing edge) are shown in Fig. 25 for $t/t_{ref} = 6$. As expected, the larger is the Pe number, the steeper is the gradient of concentration at the interface and a finer mesh is needed to resolve the boundary layer profile. In order to provide a quantitative measure of the boundary layer thickness δ_c, we use the same definition employed by Bothe and Fleckenstein (2013), who assume that δ_c is the distance from the interface where the concentration reaches the value:

$$c(\delta_c) = c_\Sigma(1 - erf(1)) \tag{74}$$

The horizontal dotted line in Fig. 25 represents the concentration value given by Eq. 74; the thickness of the different boundary layers, along with the number of cells that are contained within them, are reported in Table 7. We finally remark that adaptive mesh refinement methods are extremely useful for this class of problems, where a very fine mesh is needed only around the bubble interface.

5. Growing bubbles on electrodes

In this section we investigate the growth of electrochemically generated bubbles on planar electrodes. The production of dissolved gas at the electrode walls creates a locally supersaturated solution ($\zeta > 1$) and drives the growth of bubbles which are generated from microscopic pits on the wall surface (heterogeneous nucleation, see Pereiro et al., 2019). This phenomenon is of great relevance for the chemical engineering industry, as the presence of bubbles in electrochemical reactors can significantly reduce the performance of these devices. Bubbles are responsible for the reduction in the active area of electrodes and they induce a non uniform current distribution in the electrolytic solution. Since the gaseous phase has a much lower electrical conductivity than the

Table 4
Gas–Liquid properties.

Phase	Density $[kg/m^3]$	Viscosity $[Ns/m^2]$	Diffusivity $[m^2/s]$	Surface tension $[N/m]$	He
Liquid	1245	0.46	1.48×10^{-6}	0.06	5
Gas	1.2	1.8×10^{-5}			

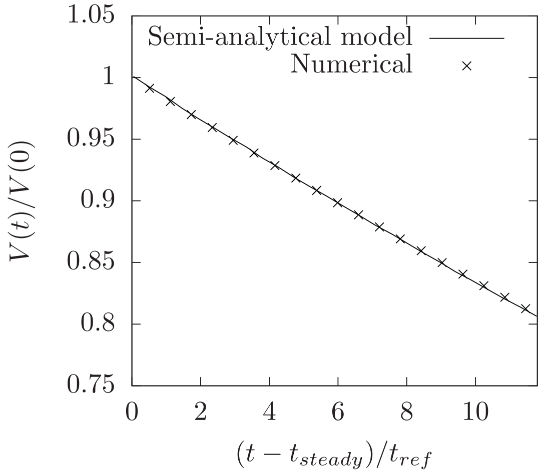

Fig. 20. Volume ratio Vs time for the rising bubble case. The simulation is first run without volume change until $t = t_{steady}$, while the full phase-change model is applied for $t > t_{steady}$.

liquid one, the presence of bubble blocks the transport of ions and the effective resistance of the electrolyte increases (Angulo et al., 2020). Here we replicate experiments carried out in Glas and Westwater (1964) for hydrogen bubbles generated on a flat electrode. A CFD study which reproduces the same experimental setup was published by Liu et al. (2016); contrary to our approach, the authors used empirical correlation models to compute the mass transfer across the interface.

The properties of the gas–liquid system are reported in Table 8. The large density ratio for this specific system ($\rho_c/\rho_d = 12450$) is observed to slow down the convergence of the multigrid solver, making the computational cost of these simulations expensive. To circumvent this problem, the gas density is increased to $\rho_d = 0.8$ kg/m^3; the molar mass is increased by the same factor, so that the volume change is not altered ($\Delta V \propto M/\rho_d$). Such change in the volume ratio does not affect the dynamics of the interface, as we limit the present study to the growth stage of bubbles attached to the wall, where the interface movement is mainly determined by the mass transfer rate. However, even for rising bubbles, the influence of such change in the density ratio is not expected to significantly affect their general dynamics (Bunner and Tryggvason, 2002).

The electrode is the flat end of a wire with a diameter of $D_e = 0.127$ mm and the bubble is initialized in our VOF simulations with the size $D_b = D_e/10$. For such small bubbles, the surface tension dominates the effect of gravity and the bubbles retain their spherical shape during the growth stage. To reduce the computational cost due to the time step limitation of the surface tension scheme, σ is decreased by a factor of 10^{-4} and gravity is set to zero. Such small surface tension is sufficient to keep the shape of the bubbles spherical for different contact angle values when no gravity is applied. When studying the growth of a single bubble on a circular electrode, the shape of the bubble and the species distribution are axisymmetric and the problem can be modelled with an axisymmetric solver (Liu et al., 2016). The domain is a square with size $L0 = 25D_b$ and the finest mesh size (AMR is used) is $LEVEL = 10$, which corresponds to ≈ 41points$/D_b$. A sketch of the case setup and mesh distribution are shown in Fig. 26. The axisymmetric condition is applied at the bottom boundary (x axis), while an outflow boundary condition is set on the right boundary; the other two boundaries are treated as walls. The initialization approach is similar to that used in Section 4.4.1, where we wait for the nucleation time of the bubble before computing the volume change. During the nucleation stage, the bubble size is kept constant, but part of the gas which is produced by the electrode is consumed at the interface. The nucleation time depends on many factors, like the electrode material, the surface finish (i.e. the size of the microscopic pits) and the current density, and cannot be estimated a priori. Here, the nucleation time is set to $t_n = 0.02$ s, which is a reasonable value, according to Glas and Westwater (1964). The molar flux of hydrogen (H_2) produced at the electrode wall is given by Faraday's law:

$$J = \frac{I}{2F} \tag{75}$$

where I is the current density applied to the electrode and F is the Faraday's constant ($F = 96485.3$ As/mol). To take into account the flux of H_2 across the active area of the electrode, a Neumann

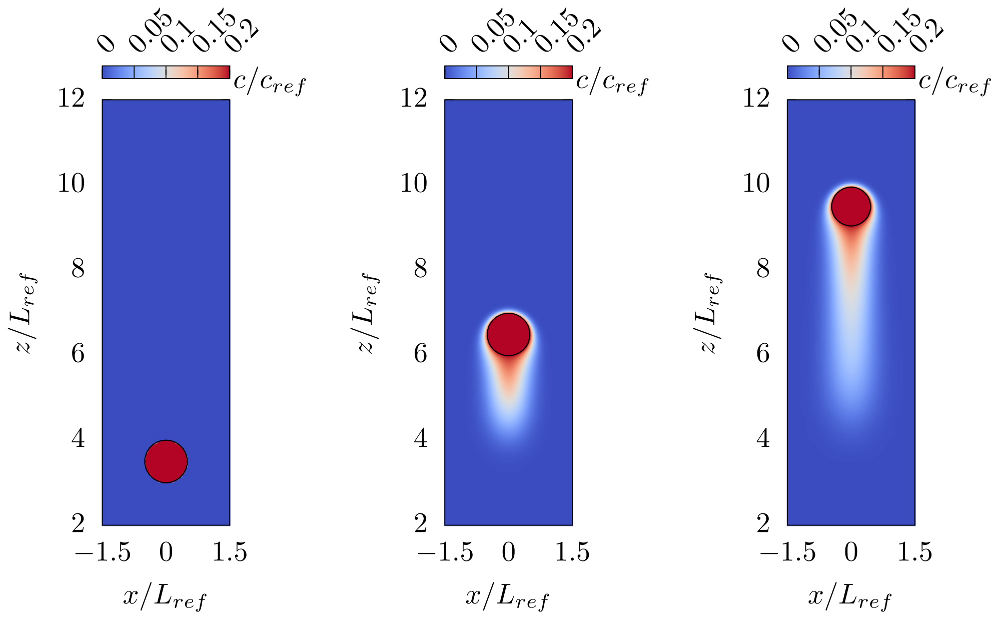

Fig. 21. Bubble position and contours of concentration at $t/t_{ref} = 0$ (left), $t/t_{ref} = 20$ (center) and $t/t_{ref} = 40$ (right).

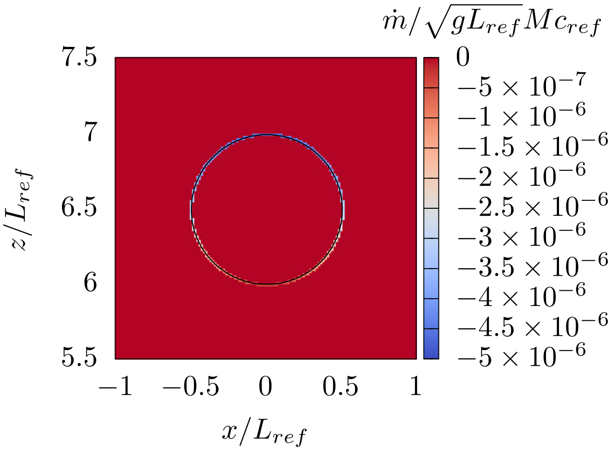

Fig. 22. Mass transfer distribution on the XZ plane. The value of $\dot{m}$ reaches its maximum on top of the bubble, where the boundary layer is thin.

boundary condition for the gas concentration is applied to the left wall (y axis):

$$\begin{array}{ll} \frac{\partial c}{\partial x} = \frac{J}{D}(1-f) & \text{for } y < \frac{D_e}{2} \\ \frac{\partial c}{\partial x} = 0 & \text{for } y > \frac{D_e}{2} \end{array} \tag{76}$$

The liquid solution is initially saturated ($\zeta = 1$). In the following, the results are reported with their dimensional units to provide a direct comparison against experimental measurements.

The first finding from the experimental work of Glas and Westwater (1964) is that the asymptotic growth of electrochemically generated bubbles follows the same functional relationship given by the solution for a suspended bubble growing in a supersaturated liquid (Scriven's model - Eq. 63) which we report here for the reader's convenience:

$$R(t) = 2\beta\sqrt{Dt}$$

Here we investigated the effect of the current density on the growth rate and the results in terms of radius evolution over time are reported in Fig. 27 for two bubbles with different contact angles θ. In both cases ($\theta = 90^\circ$ and $\theta = 35^\circ$) we found a good agreement with the proportionality law given by Scriven's model ($R(t) \propto \sqrt{t}$) for all the current densities tested here and the growth coefficient β can be derived from the slope of the linear curves fitting the numerical data.

Results from Glas and Westwater (1964) show that the variation in nucleation sites is a dominant factor which affects the growth rate of bubbles. Depending on the material and surface finishing, an electrode can have multiple nucleation sites with different sizes and the relative experimental measurements are usually affected by a significant scattering. Here we investigate the effect of the variation of nucleation sites by comparing the results obtained for a single bubble with those relative to four bubbles growing simultaneously on the electrode (3D simulation). The four bubbles are located at a distance of 0.038 mm from the electrode center and are equally spaced. The choice of modelling four nucleation sites comes from the measurements reported in Glas and Westwater (1964), where at least four sites are active. The contact angle is usually variable during the growth stage on the electrode wall; here we set $\theta = 35^\circ$ which is an average value, according to the experimental measurements. The results in terms of the influence of current density on the growth factor β are reported in Fig. 28 for the single and multiple bubble cases and are compared with the experimental measurements of Glas and Westwater (1964). The dispersion in the experiments is quite relevant especially for high current densities as more nucleation sites can be activated simultaneously and more variability is observed when the experiment is repeated. For a single nucleation site, the growth rate β is expected to increase with the current density as the amount of dissolved gas near the electrode is larger and this is confirmed by all our numerical simulations.

A nucleation site is generally a microscopic indentation on the electrode surface which traps some of the air when the cell is filled with liquid (Pereiro et al., 2019). The gas dissolved into the liquid diffuses into the gas pocket and the bubble starts to grow. If more sites are active, the gas is consumed simultaneously by all of them and the relative growth rates are smaller than for a single site, where the whole amount of gas generated by the electrode is available for the only bubble present on the wall. This mechanism explains the reason why our numerical simulations for a single site generally overpredict the experimental measurements. More interestingly, we found that the bubble with $\theta = 90^\circ$ grows faster than the $\theta = 35^\circ$ case. A possible explanation of this phenomenon is that in the $\theta = 35^\circ$ case, the bubble is more elongated in the axial direction and, therefore, less exposed to the high concentration region next to the electrode. A qualitative comparison between the $\theta = 90^\circ$ and $\theta = 35^\circ$ cases is shown in Fig. 29. As expected, the four bubble case shows smaller growth rates compared to the respective single case and the results are more consistent with the experimental measurements, confirming the relevance of the number of nucleation sites to the growth factor β.

6. Conclusion

In this work we contributed to the modelling of diffusion-driven phase-change flows by means of a geometric (PLIC) VOF scheme. A novel method is proposed to treat the velocity discontinuity at the interface which is due to the mass transfer between the phases. Our methodology consists of the redistribution of the mass transfer term from the interfacial cells to the first row of pure gas cells next to the interface and the interface area of each mixed cell is taken into account in the redistribution process. Such approach allows a liquid velocity field to be obtained which is smoothly extended across the interface and results in a divergence-free liquid velocity field, which is a fundamental requirement for incompressible VOF schemes. The advantage of our methodology is that it is readily implementable (with minimum coding effort) in existing FV codes and is compatible with any VOF scheme. The transport of species is treated with the two-scalar approach of Fleckenstein and Bothe (2015) where the advection of the species concentration is performed consistently with the transport of the volume fraction. Special attention is paid to the diffusion step, where corrections are

Table 5
Gas–Liquid properties.

Phase	Density $[kg/m^3]$	Viscosity $[Ns/m^2]$	D $[m^2/s]$	σ $[N/m]$	Sc	Pe
Liquid	998	0.005		0.06		
Gas A	1.2	1.8×10^{-5}	2×10^{-7}		25.05	465
Gas B	1.2	1.8×10^{-5}	2×10^{-8}		250.5	4650
Gas C	1.2	1.8×10^{-5}	2×10^{-9}		2505	46500

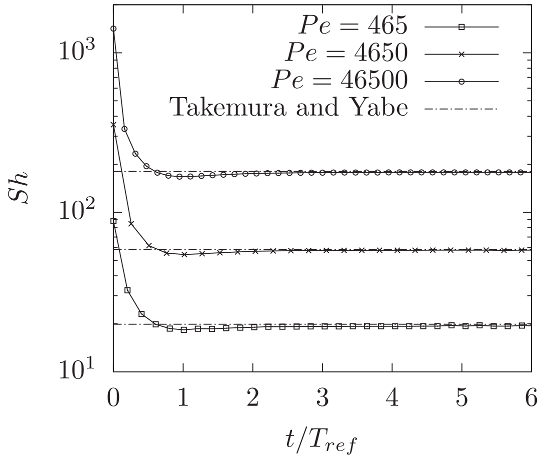

Fig. 23. Sherwood number Vs time for rising bubbles at different *Pe* numbers and comparison against the solution proposed by Takemura and Yabe (1998).

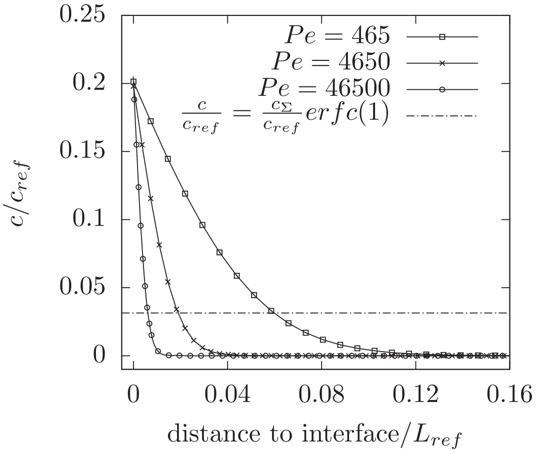

Fig. 25. Equatorial concentration profiles for rising bubbles at different *Pe* numbers. The dotted line represents the concentration value $c(\delta_c)/c_{ref}$. Profiles taken at $t/t_{ref} = 6$.

Table 6
Mesh refinements for rising bubbles at different *Pe* numbers.

Pe	Δ/L_{ref}	$\#cells/D_b$
465	7.32×10^{-3}	≈ 137
4650	1.83×10^{-3}	≈ 546
46500	4.58×10^{-4}	≈ 2185

needed to prevent any artificial diffusion across the interface of the one-sided concentration field. The whole methodology is implemented in the open source software Basilisk which uses the AMR technique to capture the smallest flow scales without the need to refine the mesh everywhere in the domain.

We performed several benchmarks to test the accuracy and correctness of the proposed methodology. The first test is a suspended bubble with a fixed mass transfer rate. This case allows the evaluation of accuracy and mass conservation properties of the redistribution algorithm and excellent agreement with the exact solution is found. The full methodology is verified against four validation tests. The first one is the well-known Stefan problem for a moving planar interface, where we obtained good accuracy for two Schmidt numbers ($Sc = 5.26$ and $Sc = 526$). The second and third tests are for expanding and collapsing bubbles, respectively. The growing case is run for three different supersaturation ratios ($\zeta = 2, \zeta = 3$ and $\zeta = 4$) and good agreement is observed with the analytical solution of Scriven. The collapsing bubble is first tested against the approximate Epstein-Plesset model for a bubble with constant size, where excellent agreement is reached. We then

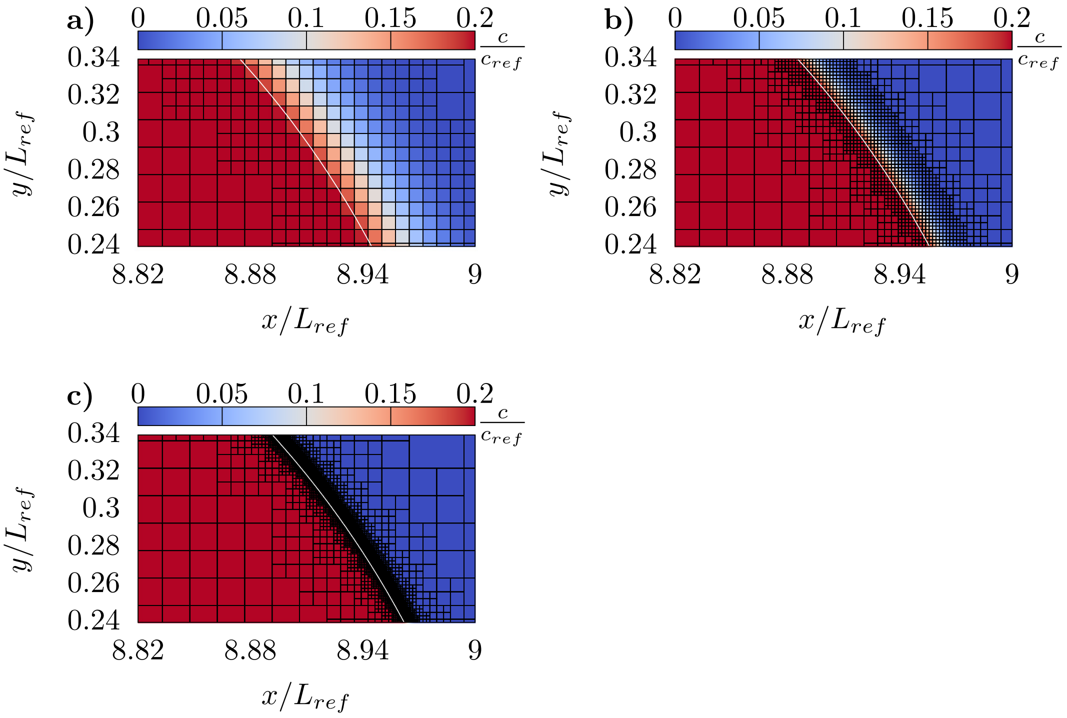

Fig. 24. Contour of gas concentration and mesh refinement for rising bubbles with $Pe = 465$ (a), $Pe = 4650$ (b) and $Pe = 46500$ (c). The withe line represents the interface. Snapshots taken at $t/t_{ref} = 6$.

run the full solution (with volume change) and we showed that the EP model deviates significantly from the numerical solution. The reason behind this discrepancy is that the EP model does not take into account the convective transport of species concentration. The equivalent numerical test without species convection shows better agreement with the EP model, until the dissolution rate becomes too fast for the quasi-stationary assumption. In the last two benchmarks we consider the dynamics of moving bubbles. First, a 3D bubble rising in a creeping flow which exchanges mass with the surrounding liquid is modelled and results are compared against the semi-analytical solution of Fleckenstein and Bothe (2015), where very good agreement is obtained. Then, the case of axisymmentric rising bubbles at different Péclet numbers is validated with the results of Takemura and Yabe (1998) and the mesh refinement needed to resolve the concentration boundary layer is discussed.

The validated approach is applied to the case of growing bubbles on planar electrodes and the results are compared with the experiments of Glas and Westwater (1964). We showed that the growth rate of bubbles follows the functional relationship of Scri-

Table 7
Equatorial boundary layer thickness for rising bubbles at different *Pe* numbers. Values taken at $t/t_{ref} = 6$.

Pe	δ_c/L_{ref}	$\#cells/\delta_c$
465	0.0598	≈ 8
4650	0.0189	≈ 10
46500	0.00612	≈ 13

Table 8
Gas–Liquid properties.

Phase	Density $[kg/m^3]$	Viscosity $[Ns/m^2]$	Diffusivity $[m^2/s]$	Surface tension $[N/m]$	*He*
Liquid	996	8.32×10^{-4}	7.38×10^{-9}	0.075	53.3
Gas	0.08	8.96×10^{-6}			

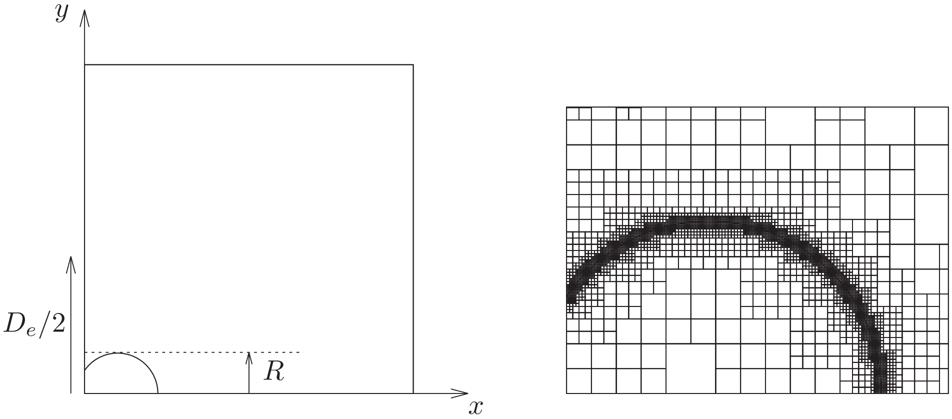

Fig. 26. Sketch of the case setup and adaptive mesh refinement around the interface.

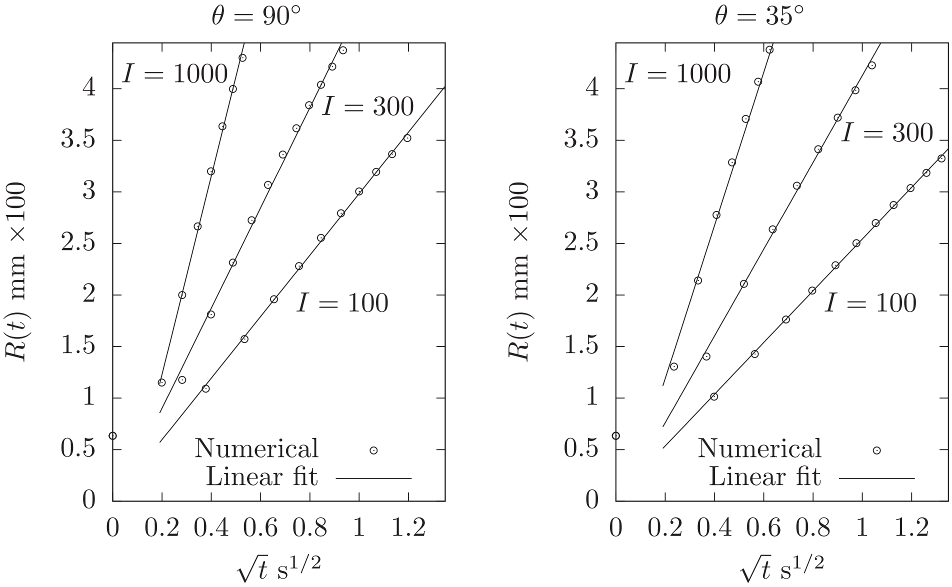

Fig. 27. Radius growth for bubbles with $\theta = 90°$ (left) and $\theta = 35°$ (right) for different current densities. The units of *I* are A/m^2.

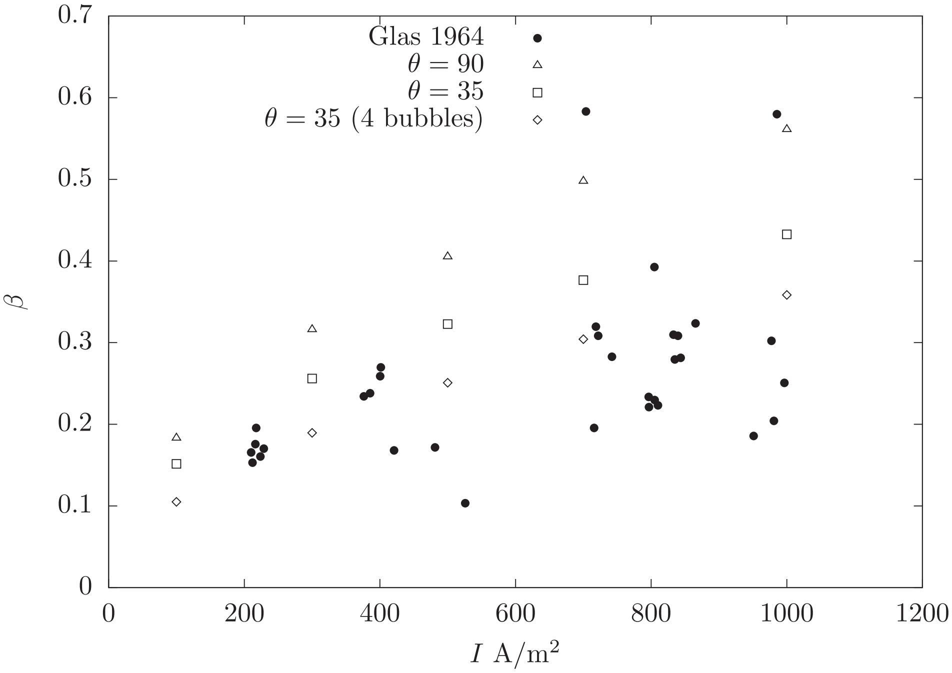

Fig. 28. Influence of current density on the growth coefficient.

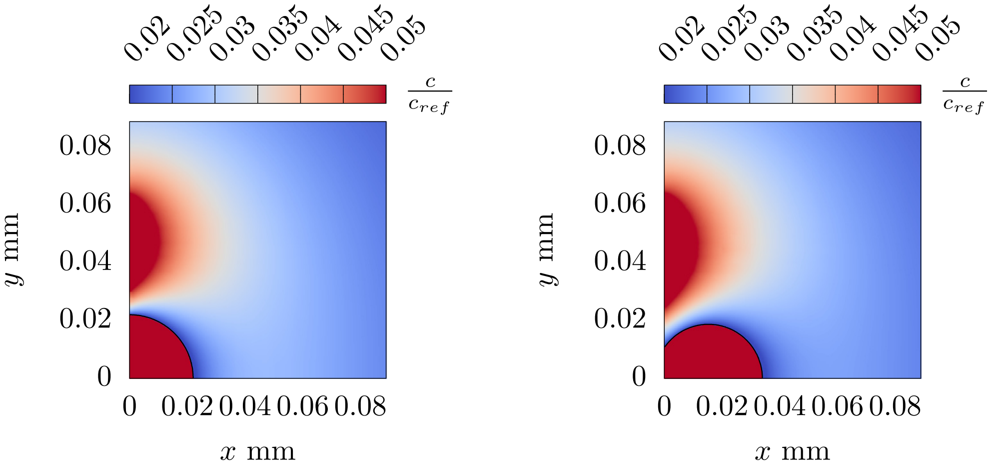

Fig. 29. Bubble shape and contour of gas concentration for $\theta = 90^\circ$ (left) and $\theta = 35^\circ$ (right) at $t = 0.53$ s.

ven ($R(t) \propto \sqrt{t}$) for different current densities, in agreement with the findings of Glas and Westwater (1964). The effect of the contact angle is shown for two different values ($\theta = 90^\circ$ and $\theta = 35^\circ$) and we found that smaller growth rates occur for the $\theta = 35^\circ$ case. The influence of the number of nucleation sites is investigated by comparing the results for single bubbles with those relative to four bubbles growing simultaneously. The average growth rate of the four bubble test is smaller than the single site case, as the amount of gas produced by the electrode is shared by all the active bubbles. Results are finally compared with the experimental campaign of Glas and Westwater (1964) and we conclude that both contact angles and number of nucleation sites must be properly taken into account when replicating experiments.

Declaration of Competing Interest

The authors declare that they have no known competing financial interests or personal relationships that could have appeared to influence the work reported in this paper.

Acknowledgments

We thank EPSRC grant EP/P013341/1 for financial support. The calculations were performed using the University of Nottingham High Performance Computing Facility and Sulis at HPC Midlands +, which was funded by EPSRC grant EP/T022108/1.

References

Alke, A., Bothe, D., Kroeger, M., Warnecke, H., 2009. Vof-based simulation of conjugate mass transfer from freely moving fluid particles. WIT Trans. Eng. Sci. 63, 157–168.

Angulo, A., van der Linde, P., Gardeniers, H., Modestino, M., Fernández Rivas, D., 2020. Influence of bubbles on the energy conversion efficiency of electrochemical reactors. Joule 4, 555–579. https://doi.org/10.1016/j.joule.2020.01.005.

Bell, J.B., Colella, P., Glaz, H.M., 1989. A second order projection method for the incompressible navier-stokes equations. J. Comput. Phys. 85, 257.

Bothe, D., Fleckenstein, S., 2013. A volume-of-fluid-based method for mass transfer processes at fluid particles. Chem. Eng. Sci. 101, 283–302. https://doi.org/10.1016/j.ces.2013.05.029.

Bothe, D., Koebe, M., Wielage, K., Prüss, J., Warnecke, H.J., 2004. Direct numerical simulation of mass transfer between rising gas bubbles and water. In: Sommerfeld, M. (Ed.), Bubbly Flows: Analysis, Modelling and Calculation. Springer Berlin Heidelberg, Berlin, Heidelberg, pp. 159–174. https://doi.org/10.1007/978-3-642-18540-3_13.

Brackbill, J.U., Kothe, D.B., Zemach, C., 1992. A continuum method for modeling surface tension. J. Comput. Phys. 100, 335–354. https://doi.org/10.1016/0021-9991(92)90240-Y.

Bunner, B., Tryggvason, G., 2002. Dynamics of homogeneous bubbly flows part 1. rise velocity and microstructure of the bubbles. J. Fluid Mech. 466, 17–52. https://doi.org/10.1017/S0022112002001179.

Clift, R., Grace, J.R., Weber, M.E., 1978. Bubbles, drops, and particles.

Crank, J., 1975. The mathematics of diffusion/ by J. Crank. Oxford science publications., Clarendon Press, Oxford [England].

Dani, A., Guiraud, P., Cockx, A., 2007. Local measurement of oxygen transfer around a single bubble by planar laser-induced fluorescence. Chem. Eng. Sci. 62, 7245–7252. https://doi.org/10.1016/j.ces.2007.08.047.

Deising, D., Marschall, H., Bothe, D., 2016. A unified single-field model framework for volume-of-fluid simulations of interfacial species transfer applied to bubbly flows. Chem. Eng. Sci. 139, 173–195. https://doi.org/10.1016/j.ces.2015.06.021.

Duda, J.L., Vrentas, J.S., 1971. Heat or mass transfer-controlled dissolution of an isolated sphere. Int. J. Heat Mass Transf. 14, 395–407. https://doi.org/10.1016/0017-9310(71)90159-1.

Duncan, P.B., Needham, D., 2004. Test of the epstein-plesset model for gas microparticle dissolution in aqueous media: Effect of surface tension and gas undersaturation in solution. Langmuir 20, 2567–2578. https://doi.org/10.1021/la034930i.

Epstein, P.S., Plesset, M.S., 1950. On the stability of gas bubbles in liquid-gas solutions. J. Chem. Phys. 18, 1505–1509. https://doi.org/10.1063/1.1747520.

Fedkiw, R.P., Aslam, T., Merriman, B., Osher, S., 1999. A non-oscillatory eulerian approach to interfaces in multimaterial flows (the ghost fluid method). J. Comput. Phys. 152, 457–492. https://doi.org/10.1006/jcph.1999.6236.

Fleckenstein, S., Bothe, D., 2015. A volume-of-fluid-based numerical method for multi-component mass transfer with local volume changes. J. Comput. Phys. 301, 35–58. https://doi.org/10.1016/j.jcp.2015.08.011.

Francois, J., Dietrich, N., Guiraud, P., Cockx, A., 2011. Direct measurement of mass transfer around a single bubble by micro-plifi. Chem. Eng. Sci. 66, 3328–3338. https://doi.org/10.1016/j.ces.2011.01.049.

Glas, J.P., Westwater, J.W., 1964. Measurements of the growth of electrolytic bubbles. Int. J. Heat Mass Transf. 7, 1427–1443. https://doi.org/10.1016/0017-9310(64)90130-9.

Guo, L., 2020. Numerical investigation of Taylor bubble and development of phase change model. Université de Lyon, Thesis. URL: https://tel.archives-ouvertes.fr/tel-03177304.

Hadamard, J., 1911. Mouvement permanent lent d'une sphére liquide et visqueuse dans un liquide visqueux. C.R. Acad. Sci. Paris 152, 1735–1738.

Hardt, S., Wondra, F., 2008. Evaporation model for interfacial flows based on a continuum-field representation of the source terms. J. Comput. Phys. 227, 5871–5895. https://doi.org/10.1016/j.jcp.2008.02.020.

Haroun, Y., Legendre, D., Raynal, L., 2010. Volume of fluid method for interfacial reactive mass transfer: Application to stable liquid film. Chem. Eng. Sci. 65, 2896–2909.

Hirt, C.W., Nichols, B.D., 1981. Volume of fluid (vof) method for the dynamics of free boundaries. J. Comput. Phys. 39, 201–225. https://doi.org/10.1016/0021-9991(81)90145-5.

van Hooft, J.A., Popinet, S., van Heerwaarden, C.C., van der Linden, S.J.A., de Roode, S. R., van de Wiel, B.J.H., 2018. Towards adaptive grids for atmospheric boundary-layer simulations. Bound.-Layer Meteorol. 167, 421–443. https://doi.org/10.1007/s10546-018-0335-9.

Kumar Farsoiya, P., Popinet, S., Deike, L., 2021. Bubble-mediated transfer of dilute gas in turbulence. J. Fluid Mech.

Kunkelmann, C., Stephan, P., 2009. Cfd simulation of boiling flows using the volume-of-fluid method within openfoam. Numerical Heat Transfer, Part A: Applications 56, 631–646. https://doi.org/10.1080/10407780903423908.

Liu, H.b., Pan, L.m., Wen, J., 2016. Numerical simulation of hydrogen bubble growth at an electrode surface. Canadian Journal of Chemical Engineering 94, 192–199.

López-Herrera, J.M., Gañán-Calvo, A.M., Popinet, S., Herrada, M.A., 2015. Electrokinetic effects in the breakup of electrified jets: A volume-of-fluid numerical study. Int. J. Multiph. Flow 71, 14–22. https://doi.org/10.1016/j.ijmultiphaseflow.2014.12.005.

Ma, C., Bothe, D., 2013. Numerical modeling of thermocapillary two-phase flows with evaporation using a two-scalar approach for heat transfer. J. Comput. Phys. 233, 552–573. https://doi.org/10.1016/j.jcp.2012.09.011.

Maes, J., Soulaine, C., 2018. A new compressive scheme to simulate species transfer across fluid interfaces using the volume-of-fluid method. Chem. Eng. Sci. 190, 405–418. https://doi.org/10.1016/j.ces.2018.06.026.

Maes, J., Soulaine, C., 2020. A unified single-field volume-of-fluid-based formulation for multi-component interfacial transfer with local volume changes. J. Comput. Phys. 402, 109024. https://doi.org/10.1016/j.jcp.2019.109024.

Magnini, M., Pulvirenti, B., Thome, J.R., 2013. Numerical investigation of hydrodynamics and heat transfer of elongated bubbles during flow boiling in a microchannel. Int. J. Heat Mass Transf. 59, 451–471. https://doi.org/10.1016/j.ijheatmasstransfer.2012.12.010.

Malan, L.C., Malan, A.G., Zaleski, S., Rousseau, P.G., 2021. A geometric vof method for interface resolved phase change and conservative thermal energy advection. J. Comput. Phys. 426, 109920. https://doi.org/10.1016/j.jcp.2020.109920.

Marschall, H., Hinterberger, K., Schüler, C., Habla, F., Hinrichsen, O., 2012. Numerical simulation of species transfer across fluid interfaces in free-surface flows using openfoam. Chem. Eng. Sci. 78, 111–127. https://doi.org/10.1016/j.ces.2012.02.034.

Nguyen, D.Q., Fedkiw, R.P., Kang, M., 2001. A boundary condition capturing method for incompressible flame discontinuities. J. Comput. Phys. 172, 71–98. https://doi.org/10.1006/jcph.2001.6812.

Pereiro, I., Fomitcheva Khartchenko, A., Petrini, L., Kaigala, G.V., 2019. Nip the bubble in the bud: a guide to avoid gas nucleation in microfluidics. Lab Chip 19, 2296–2314. https://doi.org/10.1039/C9LC00211A.

Popinet, S., 2003. Gerris: a tree-based adaptive solver for the incompressible euler equations in complex geometries. J. Comput. Phys. 190, 572–600. https://doi.org/10.1016/S0021-9991(03)00298-5.

Popinet, S., 2009. An accurate adaptive solver for surface-tension-driven interfacial flows. J. Comput. Phys. 228, 5838–5866. https://doi.org/10.1016/j.jcp.2009.04.042.

Popinet, S., 2015. A quadtree-adaptive multigrid solver for the serre–green–naghdi equations. J. Comput. Phys. 302, 336–358. https://doi.org/10.1016/j.jcp.2015.09.009.

Popinet, S., 2018. Numerical models of surface tension. Annu. Rev. Fluid Mech. 50, 49–75. https://doi.org/10.1146/annurev-fluid-122316-045034.

Popinet, S., collaborators, 2013–2022. Basilisk. http://basilisk.fr.

Rybczynski, W., 1911. On the translatory motion of a fluid sphere in a viscous medium. Bull. Acad. Sci. Cracovie, 40–46.

Scapin, N., Costa, P., Brandt, L., 2020. A volume-of-fluid method for interface-resolved simulations of phase-changing two-fluid flows. J. Comput. Phys. 407, 109251. https://doi.org/10.1016/j.jcp.2020.109251.

Scardovelli, R., Zaleski, S., 1999. Direct numerical simulation of free-surface and interfacial flow. Annu. Rev. Fluid Mech. 31, 567–603. https://doi.org/10.1146/annurev.fluid.31.1.567.

Schlottke, J., Weigand, B., 2008. Direct numerical simulation of evaporating droplets. J. Comput. Phys. 227, 5215–5237. https://doi.org/10.1016/j.jcp.2008.01.042.

Schulz, A., Wecker, C., Inguva, V., Lopatin, A.S., Kenig, E.Y., 2022. A plic-based method for species mass transfer at free fluid interfaces. Chem. Eng. Sci. 251, 117357. https://doi.org/10.1016/j.ces.2021.117357.

Scriven, L.E., 1959. On the dynamics of phase growth. Chem. Eng. Sci. 10, 1–13. https://doi.org/10.1016/0009-2509(59)80019-1.

Sharaborin, E.L., Rogozin, O.A., Kasimov, A.R., 2021. The coupled volume of fluid and brinkman penalization methods for simulation of incompressible multiphase flows. Fluids 6, 334.

Magdelaine-Guillot de Suduiraut, Q., 2019. Hydrodynamique des films liquides hétérogènes. Thesis. Sorbonne université. URL: http://www.theses.fr/2019SORUS531/document.

Sussman, M., 2003. A second order coupled level set and volume-of-fluid method for computing growth and collapse of vapor bubbles. J. Comput. Phys. 187, 110–136. https://doi.org/10.1016/S0021-9991(03)00087-1.

Sussman, M., Smereka, P., Osher, S., 1994. A level set approach for computing solutions to incompressible two-phase flow. J. Comput. Phys. 114, 146–159. https://doi.org/10.1006/jcph.1994.1155.

Takemura, F., Matsumoto, Y., 2000. Dissolution rate of spherical carbon dioxide bubbles in strong alkaline solutions. Chem. Eng. Sci. 55, 3907–3917. https://doi.org/10.1016/S0009-2509(00)00022-1.

Takemura, F., Yabe, A., 1998. Gas dissolution process of spherical rising gas bubbles. Chem. Eng. Sci. 53, 2691–2699. https://doi.org/10.1016/S0009-2509(98)00094-3.

Takemura, F., Yabe, A., 1999. Rising speed and dissolution rate of a carbon dioxide bubble in slightly contaminated water. J. Fluid Mech. 378, 319–334. https://doi.org/10.1017/S0022112098003358.

Tanguy, S., Ménard, T., Berlemont, A., 2007. A level set method for vaporizing two-phase flows. J. Comput. Phys. 221, 837–853. https://doi.org/10.1016/j.jcp.2006.07.003.

Taqieddin, A., Liu, Y., Alshawabkeh, A.N., Allshouse, M.R., 2020. Computational modeling of bubbles growth using the coupled level set–volume of fluid method. Fluids 5, 120.

Tripathi, M.K., Sahu, K.C., Govindarajan, R., 2015. Dynamics of an initially spherical bubble rising in quiescent liquid. Nature Communications 6, 6268. https://doi.org/10.1038/ncomms7268.

Tryggvason, G., Bunner, B., Esmaeeli, A., Juric, D., Al-Rawahi, N., Tauber, W., Han, J., Nas, S., Jan, Y.J., 2001. A front-tracking method for the computations of multiphase flow. J. Comput. Phys. 169, 708–759. https://doi.org/10.1006/jcph.2001.6726.

Tryggvason, G., Scardovelli, R., Zaleski, S., 2011. Direct Numerical Simulations of Gas–Liquid Multiphase Flows. Cambridge University Press, Cambridge. doi:DOI: 10.1017/CBO9780511975264.

Vachaparambil, K.J., Einarsrud, K.E., 2020. Numerical simulation of bubble growth in a supersaturated solution. Appl. Math. Model. 81, 690–710. https://doi.org/10.1016/j.apm.2020.01.017.

Welch, S.W.J., Wilson, J., 2000. A volume of fluid based method for fluid flows with phase change. J. Comput. Phys. 160, 662–682. https://doi.org/10.1006/jcph.2000.6481.

Weymouth, G.D., Yue, D.K.P., 2010. Conservative volume-of-fluid method for free-surface simulations on cartesian-grids. J. Comput. Phys. 229, 2853–2865. https://doi.org/10.1016/j.jcp.2009.12.018.

Youngs, D.L., 1984. An interface tracking method for a 3D Eulerian hydrodynamics code. Report 44/92/35. AWRE.

Zanutto, C.P., Evrard, F., van Wachem, B., Denner, F., Paladino, E.E., 2022a. Modeling interfacial mass transfer of highly non-ideal mixtures using an algebraic vof method. Chem. Eng. Sci. 251, 117458. https://doi.org/10.1016/j.ces.2022.117458.

Zanutto, C.P., Paladino, E.E., Evrard, F., van Wachem, B., Denner, F., 2022b. Modeling of interfacial mass transfer based on a single-field formulation and an algebraic vof method considering non-isothermal systems and large volume changes. Chem. Eng. Sci. 247, 116855. https://doi.org/10.1016/j.ces.2021.116855.